Human-aware localization using linear-frequency-modulated continuous-wave radars

5

J.-M. Muñoz-Ferreras[1], R. Gómez-García[1] and C. Li[2]

[1]*University of Alcalá, Madrid, Spain* [2]*Texas Tech University, Lubbock, TX, United States*

CHAPTER OUTLINE

5.1 INTRODUCTION

Nowadays, short-range radars are emerging as interesting devices for indoor and outdoor applications [1−6]. Non-contact human-aware localization can be attained through these radar sensors, which must be compact and have good performance [7−10]. Applications range from eldercare, patient monitoring, detection of surviving people after avalanches or earthquakes, and real-time healthcare to radar-based augmented reality [11−16].

To this purpose, two main architectures have traditionally been proposed in the literature: Doppler radars and impulse radio ultra-wideband (IR-UWB) radar systems. The former employ a single tone as the transmitting waveform, not possessing range resolution [11,17,18]. The latter transmit extremely narrow pulses which are usually difficult to acquire [12,19−22]. In both cases, many schemes and associated processing approaches have been suggested with interesting and promising results in the field of biosensing and healthcare [17−22].

This chapter is devoted to the recently suggested linear-frequency-modulated continuous-wave (LFMCW) radar architecture for human-aware localization applications [7,23−26]. By also adding the coherence feature, the system combines an excellent phase-based precision in the range measurements of targets with the disposition of range resolution [23−26]. Additionally, the acquisition of the echoes returned from the targets can be largely simplified, which can be exploited to develop inexpensive radar prototypes [23−26].

The chapter is written in a self-contained style, so that the reader can find all the important information to understand, construct, use, and even simulate a coherent LFMCW radar prototype for short-range applications. Given its unique features, it is the opinion of the authors that this kind of radar system will proliferate in the near future to improve our quality of life. Perhaps, the automotive sector is currently leading this race [27−29].

The next section describes the so-called deramping technique, which is the key concept for a low-cost LFMCW radar. It consists in mixing a replica of the transmitted signal with the echoes coming from the targets.

An easy-to-follow mathematical analysis to understand the signal waveforms is introduced in Section 5.3, which provides the reader with important concepts,

such as fast-time, slow-time, range resolution, and so forth. Section 5.3 also details key aspects related to the coherence maintenance of the radar, so that the phase/Doppler history of the target scatterers can be exploited. Additionally, two simple algorithms to obtain the range evolution of targets are introduced. Respectively based on the amplitude and the phase of the slow-time signal, these algorithms can be employed to derive the range history of targets, which is the main output required in human-aware localization applications.

Signal processing issues are provided in Section 5.4, with the introduction of the conventional data formatting and the construction of important matrices, such as the range-profile matrix or the range-Doppler map. Also, a more formal description of the algorithms to track the range history of targets is provided in Section 5.4.

Section 5.5 reviews the important concepts of range resolution, precision, and accuracy in the context of coherent LFMCW radars. The authors have noted that sometimes these concepts are not adequately used in the literature, which usually leads the reader to confusion. The concepts are also briefly described for other dimensions, such as angle (azimuth or elevation) and Doppler.

On other hand, clutter is any unwanted return which may have a negative impact on the correct working of the radar. In a context of human-aware localization, Section 5.6 provides a mathematical framework for possibly arising clutter effects and the proposal of Doppler-based mitigation techniques for coherent LFMCW radars.

Simulated and experimental results are respectively given in Sections 5.7 and 5.8. Simulated examples enable corroboration of the principle of operation of the radar system, the implied mathematics, the indicated limitations, and the proposed algorithms. Experimental results also confirm the concepts and make the connection with reality. Additionally, a description of the constructed prototype is briefly provided.

The final section (Section 5.9) briefly suggests our future work, which is mainly concentrated on the construction of a millimeter-wave coherent LFMCW prototype. The advantages of increasing the operation frequency of the radar sensor are commented on in Section 5.9.

5.2 LFMCW RADAR ARCHITECTURE

A radar is a microwave/RF (radio frequency) system which incorporates a transmission (Tx) and a reception (Rx) chain. It is able to generate signals to be transmitted into the air and to capture the echoes returned from the targets. Fig. 5.1 shows a general scheme for any radar [30,31].

In the Tx part, an important block is the signal generation stage, which is responsible for the correct generation of the waveform to be transmitted. The generation block usually works at baseband and is conventionally made up of a direct
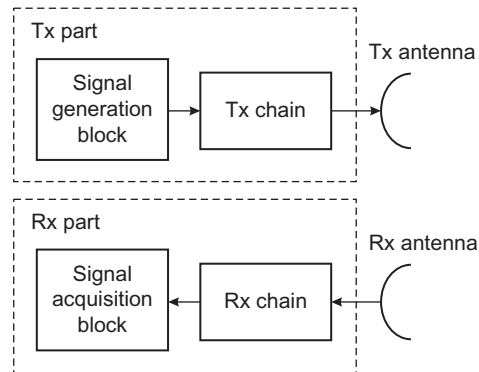
FIGURE 5.1

General two-antenna architecture for radar systems.

digital synthesizer (DDS), which generates the samples corresponding to the desired waveform. To avoid spectral aliasing, the output of the DDS is filtered with a low-pass profile with a cut-off frequency in the range of the sampling frequency. The Tx chain is responsible for upconverting the baseband signal to the RF range, in which the Tx to the air is possible. This signal conditioning is made through mixers and/or frequency multipliers. The Tx chain also possesses amplifiers and filters to further enhance the spectrum to be transmitted. One important element in the Tx chain is the usually-last high power amplifier, which increases the level of the output signal so that the range of the radar to detect far targets can be improved [30,31].

Fig. 5.1 shows that the transmitter uses a specific antenna, different from the one in the Rx part. This two-antenna scheme is usually preferred in continuous-wave (CW) radar prototypes, since for this case, the transmitter is operating all the time, and the Tx−Rx isolation must be large so that the high levels in the Tx part cannot damage the sensitive receiver. A scheme based on a single antenna (not shown in Fig. 5.1) must employ a bulky circulator and a limiter in the Rx chain to attain protective Tx−Rx isolation levels. In any case, the two-antenna architecture is preferred and easily found in many LFMCW radars [32,33].

Regarding the Rx part, the microwave chain is shaped by the cascading connection of amplifiers, mixers, and filters, which achieves an adequate conditioning of the received signal. A first element in the Rx chain is usually a low-noise amplifier (LNA), which permits the increase of the sensitivity of the radar for weak targets, since the noise level at Rx is reduced. After one or two down-conversions from the RF stage to an intermediate frequency stage, it is usual to find an In-Phase/Quadrature (I/Q) demodulation, in which the signal is split into two branches and respectively mixed with two in-quadrature tones. The I and Q baseband channels are subsequently acquired by the signal acquisition block, which makes the corresponding sampling of these signals. The sampling process

is made through an analog-to-digital converter (ADC), which is a costly device, especially if a very high sampling frequency (f_s) is required [30,31].

If a good range resolution is desired, radars usually transmit a large bandwidth (B) (say in the range of hundreds of megahertz) [32,33]. This leads to the fact that both the Tx and Rx parts must adequately handle this wideband signal. The ADC of the acquisition block should employ a very high sampling frequency to permit the correct handling of the signal bandwidth without spectral overlapping (aliasing) [30,31]. By supposing an I/Q demodulation, the sampling frequency must satisfy the following inequality:

$$f_s \geq B. \tag{5.1}$$

In other words, according to the architecture in Fig. 5.1, a very high sampling frequency must be used if a good range resolution is required. This means that very expensive acquisition blocks should be used.

Long-range radars are expensive equipment which use complex generation and acquisition blocks. Additionally, they have to transmit large powers. On the contrary, the intended human-aware localization scenarios belong to short-range applications. The LFMCW waveform is widely employed for short-range radars and its associated architecture, based on the analog deramping technique, can circumvent the restriction imposed by Eq. (5.1), which fortunately leads to cost-effective high-resolution radar solutions.

5.2.1 DERAMPING-BASED LFMCW RADAR ARCHITECTURE

For short-range applications, the most interesting architecture for an LFMCW radar is depicted in Fig. 5.2. The key difference with respect to Fig. 5.1 is found in the RF mixing stage, in which a replica of the transmitted signal is mixed with the returned echoes. This analog processing is called deramping or dechirping [32,33].

The signal after the mixing process is the so-called beat signal, which is subsequently processed by the Rx chain. The important point is that the bandwidth of the beat signal is much lower than the transmitted one B. This means that its acquisition can be achieved by a low-end ADC, which largely simplifies the whole radar system. In particular, it will be later shown in Section 5.3 that the sampling frequency of the ADC must now meet the following constraint [32,33]:

$$f_s \geq \frac{2\gamma}{c} R_{max} \tag{5.2}$$

where γ is the chirp rate, c is the speed of light, and R_{max} is the maximum range from which echoes of targets are expected. For short ranges (say tenths of meters), the bandwidth of the beat signal (i.e., the right-hand term of Eq. 5.2) is much lower than the transmitted bandwidth B. This bandwidth reduction simplifies the radar prototype while maintaining the same range resolution.
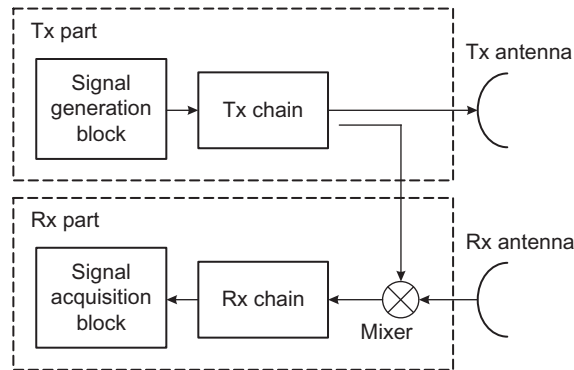
FIGURE 5.2

Scheme for an LFMCW radar based on the analog deramping technique.

This simplification of the ADC enables the transformation of these radars into quasi-commercial off-the-shelf prototypes, which are cost effective. Indeed, their development has been accomplished out of military scenarios. Examples can be found in the technical literature, such as the miniaturized Miniaturized Synthetic Aperture Radar (MiSAR) developed to fly on small unmanned aerial vehicles [34], the millimeter wave high-range-resolution Technical University of Madrid prototype [35], the Brigham Young University μSAR systems [36,37], or the X-band Delft University of Technology demonstrator [38]. Also, deramping-based LFMCW prototypes can be found for automotive radars [27−29].

5.3 LFMCW WAVEFORM

Fig. 5.3 shows a representation of the instantaneous frequency for the LFMCW waveform [25]. As can be seen, the frequency varies linearly in each period T. This is the typical behavior for a chirp, whose amplitude versus time plotting is also depicted in Fig. 5.3. The transmitted bandwidth is given by the parameter B, whereas the center transmitted frequency is f_c. The inverse of the period T is historically referred to as the pulse repetition frequency (PRF), although the LFMCW waveform is not a pulsed signal.

CW radars continuously transmit a signal. This implies that the receiver is opened for all of the time and can integrate more energy in comparison with pulsed radars, in which the energy is concentrated in short pulses and limited in Tx (i.e., it is very costly to obtain high peak powers in pulsed radars). This feature of CW radars leads to a better signal-to-noise ratio (SNR), which ultimately implies a better performance (e.g., in terms of range precision) [30,31].

The LFMCW waveform inherits this advantage from its CW nature, but additionally it provides range resolution due to the transmitted bandwidth B.
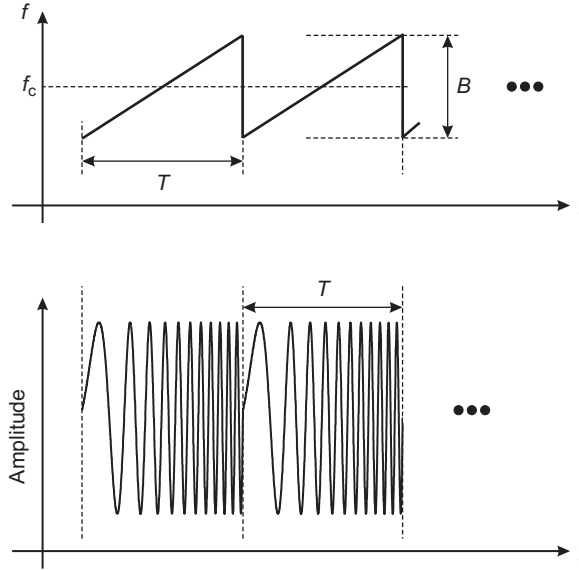
FIGURE 5.3

Transmitted waveform for an LFMCW radar. Instantaneous frequency versus time, and amplitude versus time.

The range resolution (which is higher when the transmitted bandwidth B is larger) confers interesting range-isolation properties upon LFMCW radar systems.

5.3.1 MATHEMATICAL ANALYSIS

The LFMCW waveform can be mathematically treated. Important concepts (such as range resolution, sampling requirements, phase history, Doppler, etc.) emerge from this analysis. Also, this mathematics is important for understanding the associated signal processing methods, such as the construction of the raw-data matrix or the phase-based range tracking of an isolated target [25].

In one waveform period T, the expression for the transmitted complex analytic signal can be expressed as

$$s_{\mathrm{Tx}}(t) = \exp\left(j(2\pi f_{\mathrm{c}}t + \pi\gamma t^2)\right) \tag{5.3}$$

where f_{c} is the central frequency (refer to Fig. 5.3), γ is the chirp rate (i.e., the slope of the linear frequency-time curve in Fig. 5.3), and t is the "fast-time" that must be defined in the interval $[-T/2,\ T/2]$. The chirp rate γ can be easily shown to be

$$\gamma = \frac{B}{T} = B \cdot \mathrm{PRF}. \tag{5.4}$$

Note that the instantaneous frequency of the signal Eq. (5.3) can be calculated as

$$f_{Tx}(t) = \frac{1}{2\pi} \frac{d\phi_{Tx}(t)}{dt} = f_c + \gamma t \tag{5.5}$$

where the phase $\varphi_{Tx}(t)$ is the phase corresponding to Eq. (5.3). That is,

$$\phi_{Tx}(t) = 2\pi f_c t + \pi \gamma t^2. \tag{5.6}$$

According to Eq. (5.5) and to the fact that the fast-time t is defined in the interval $[-T/2, T/2]$, the instantaneous frequency linearly sweeps from $f_c - \gamma T/2$ to $f_c + \gamma T/2$. This speaks of the importance of defining the fast-time t in the interval $[-T/2, T/2]$ so that the parameter f_c is indeed the center frequency. Also, note the distinction between fast-time and time. The time varies continuously, whereas the fast-time t is always defined in the interval $[-T/2, T/2]$ for every waveform period T.

Suppose a target whose range to the radar is given by $R(\tau)$, where τ is the so-called "slow-time." The target is assumed to be a point scatterer and the slow-time τ is assumed to be discretized at T intervals. That means that the slow-time τ only takes values at 0, T, $2T$, and so forth, so that the slow-time naturally appears sampled at the rate PRF. In other words, the range $R(\tau)$ is assumed to be constant during each interval T, or the target is assumed to hop from its past position to its current location instantaneously. Obviously, this does not reflect a realistic smooth motion of the target, but this so-called "stop-and-go" or "stop-and-hop" approximation is excellent for slow targets (such as the ones considered in this chapter) and drastically simplifies the mathematical analysis of radar signals [30−33]. Furthermore, the stop-and-go hypothesis is intrinsic to every single piece of work in the field of radar signal processing, such as algorithms for synthetic aperture radar (SAR) imagery or conventional moving target indicator (MTI) processing for long-range surveillance radars [30−33]. In any case, works beyond the stop-and-hop assumption can be found in the literature when dealing with fast targets, and its violation leads to unexpected effects, such as the range broadening for the blades of a helicopter [39].

The signal reflected from the point scatterer in the interval T can be simply written as

$$s_{Rx}(t) = \sigma \cdot s_{Tx}\left(t - \frac{2R(\tau)}{c}\right) \tag{5.7}$$

where σ is the amplitude of the received signal with respect to the amplitude of the transmitted signal, which was assumed to be the unity. This amplitude obviously depends on the distance of the target to the radar, propagation losses, additional losses in the microwave chains, antenna pointing errors, and the radar cross section of the target.

At the output of the RF mixer in the deramping-based architecture in Fig. 5.2, the beat signal $s_b(t)$ arises. By combining Eqs. (5.3) and (5.7), the mathematical form for $s_b(t)$ can be written as

$$s_b(t) = s_{Tx}(t) \cdot s_{Rx}^*(t) = \sigma \cdot \exp\left(j\left(\frac{4\pi\gamma R(\tau)}{c}t + \frac{4\pi f_c R(\tau)}{c} + \phi_{RVP}\right)\right) \qquad (5.8)$$

where φ_{RVP} is the so-called residual video phase [32]

$$\phi_{RVP} = -\frac{4\pi\gamma R^2(\tau)}{c^2}. \qquad (5.9)$$

The term φ_{RVP} in Eq. (5.9) is negligible for short ranges (note that the speed of light appears squared in the denominator), and thus, it is usually disregarded (and assumed to be zero in the next equations) [32]. By taking a look at Eq. (5.8), one concludes that the beat signal for a point-scatterer target for the period T is a sinusoidal signal whose fast-time frequency (beat frequency f_b) is given by

$$f_b(\tau) = \frac{1}{2\pi}\frac{d\phi_b(t)}{dt} = \frac{2\gamma R(\tau)}{c} \qquad (5.10)$$

where the phase of the beat signal $\varphi_b(\tau)$, from Eq. (5.8), is

$$\phi_b(t) = \frac{4\pi\gamma R(\tau)}{c}t + \frac{4\pi f_c R(\tau)}{c}. \qquad (5.11)$$

That is, in each slow-time instant (for which the target is assumed to be static at the range position $R(\tau)$), the beat frequency is constant and given by Eq. (5.10). It comes to light that a Fourier transform of the beat signal (Eq. 5.8) gives rise to a spectrum with a single peak (corresponding to the single point-scatterer target) at f_b. According to Eq. (5.10), the frequency of the beat signal is proportional to the range, so that a simple scaling can transform the frequency axis to a range axis; hence the "range profile" can be obtained (one range profile for each period T of the LFMCW waveform). Note that this range profile provides the range positions of the illuminated scatterers, since the beat signal for many targets is simply the sum of the corresponding signals for each scatterer Eq. (5.8).

Regarding the acquisition of the beat signal, it comes to light that the maximum beat frequency, according to Eq. (5.10), can be expressed as

$$f_{b,max} = \frac{2\gamma R_{max}}{c} \qquad (5.12)$$

where R_{max} is the maximum range from which echoes are expected to come. Assuming that the beat signal is a complex-valued function (i.e., it comes from an I/Q demodulation), Eq. (5.2) is demonstrated. This means that the ADC for the deramping-based architecture (Fig. 5.2) can use a low sampling frequency, which largely simplifies the radar prototype. In other words, for short-range LFMCW radars, it happens that

$$f_{b,max} \ll B. \qquad (5.13)$$

As an example, consider that $R_{\max} = 30$ m, $B = 1$ GHz, and $T = 1$ ms. The chirp rate (see Eq. 5.4) is $\gamma = 10^{12}$ Hz/seconds. From Eq. (5.12), the maximum beat frequency Eq. (5.12) is only $f_{b,\max} = 200$ kHz, which is much lower than the transmitted bandwidth ($B = 1$ GHz).

The fast-time Fourier transform $S_b(f)$ of Eq. (5.8) (i.e., the mathematical expression for the range profile) can be easily shown to be

$$S_b(f) = \sigma T \cdot \exp\left(j\frac{4\pi f_c R(\tau)}{c} \right) \cdot \operatorname{sinc}\left(T\left(f - \frac{2\gamma R(\tau)}{c} \right) \right) \qquad (5.14)$$

where

$$\operatorname{sinc}(x) = \frac{\sin(\pi \cdot x)}{\pi \cdot x}. \qquad (5.15)$$

The frequency f is the Fourier variable associated with the fast-time t. As seen in Eq. (5.14), the sinc function appears centered at the beat frequency f_b of the target (see Eq. 5.10). Additionally, as is widely known, the 3-dB width of the sinc in the f-variable is given by

$$\Delta f = \frac{1}{T}. \qquad (5.16)$$

After the aforementioned scaling to transform the f-axis into a range-axis, the width of the sinc (i.e., the width of the point spread function (PSF) of the target or the range resolution) can be written as

$$\Delta R = \frac{c}{2\gamma}\Delta f = \frac{c}{2\gamma} \cdot \frac{1}{T} = \frac{c}{2B}. \qquad (5.17)$$

The right-hand term in Eq. (5.17) is general for the range resolution of any radar. It says that a higher resolution can be attained if the transmitted instantaneous bandwidth B is increased. As is further explained in Section 5.5.1, the range resolution is the ability of the radar to discriminate two targets closely spaced in range. For example, a high range resolution (HRR) radar transmits a large bandwidth so that the targets become "extended targets"; i.e., a single target appears in many range resolution cells [33]. A bandwidth B of 1 GHz implies a range resolution $\Delta R = 15$ cm. In the particular case of a deramping-based LFMCW short-range radar, the resolution is still given by Eq. (5.17). The clear advantage is that the acquisition block can be very simple and thus, the radar can be inexpensive, as previously anticipated in Section 5.2.

In an LFMCW radar, it is obviously necessary to apply a Fourier transform in order to obtain a range profile for each waveform period T. This Fourier transform operation is digitally performed (through a Fast Fourier Transform (FFT)) after the acquisition of the low-pass-filtered beat signal.

A clarifying statement is given next. Fig. 5.4 indicates that the beat signal Eq. (5.8) is not present during the complete T interval for all the targets. The useful interval T_u is the one which should be acquired and processed, which implies that the processed effective bandwidth B_{eff} is slighter lower than the transmitted
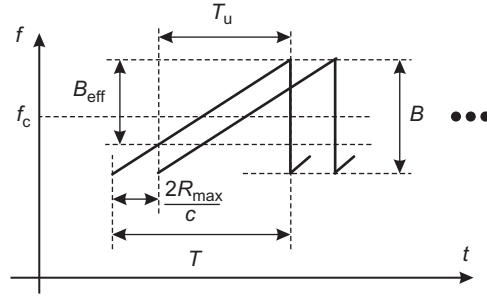
FIGURE 5.4

Definition of the useful interval and the effective bandwidth for an LFMCW radar.

bandwidth B. All the expressions in this section should be modified by writing T_u instead of T, and B_{eff} instead of B. In any case, note that the useful interval T_u is given by

$$T_u = T - \frac{2R_{max}}{c} \tag{5.18}$$

which is only slightly lower than the period T for an LFMCW short-range radar. For example, if $T = 1$ ms and $R_{max} = 30$ m, the difference $T - T_u$ is only 0.2 µs.

5.3.2 COHERENCE MAINTENANCE

The Doppler frequency (f_{Dop}) of a moving target illuminated by a radar is well-known to be [30−33]

$$f_{Dop} = \frac{2v_{rad}}{\lambda} \tag{5.19}$$

where v_{rad} is the radial velocity of the target (i.e., the speed component along the radar line-of-sight (LOS) vector) and λ is the wavelength associated with the center frequency, whose expression is

$$\lambda = \frac{c}{f_c}. \tag{5.20}$$

A convention for the sign of the Doppler frequency is usually followed. It says that the Doppler is positive if the target is approaching the radar, and negative when the target is moving away.

Regarding the LFMCW waveform, if one takes a look at Eq. (5.14), it is noticeable that the range profile for a point scatterer is shaped by the multiplication of an exponential factor and a sinc factor. The latter has profoundly been explained in the previous section; remember that it is related to the range position of the target. From range profile to range profile, it becomes clear that the target can migrate through range resolution cells (depending on its dynamics and the

value of the range resolution ΔR). In any case, this migration can be corrected by specific algorithms, such as the extended envelope correlation or global range alignment [40,41]. In relation to the former factor (the exponential one in Eq. 5.14), it turns out to represent a phase history of the target in the slow-time τ. Indeed, it becomes trivial that this phase $\varphi_t(\tau)$ is given by

$$\phi_t(\tau) = \frac{4\pi f_c R(\tau)}{c}. \tag{5.21}$$

Assume now that the range history of the target $R(\tau)$ can be written as

$$R(\tau) = R_0 + v_{rad} \cdot \tau \tag{5.22}$$

where R_0 is the initial range of the target and v_{rad} is its along-LOS speed. That is, the target is assumed to be uniformly moving. For this particular case and according to Eq. (5.21), the phase history of the target is

$$\phi_t(\tau) = \frac{4\pi f_c}{c}(R_0 + v_{rad} \cdot \tau). \tag{5.23}$$

In other words, the exponential factor of Eq. (5.14) is a sinusoidal signal in the slow-time τ with a frequency f_{Dop}, given by

$$f_{Dop} = \frac{1}{2\pi}\frac{d\phi_t(\tau)}{d\tau} = \frac{2f_c v_{rad}}{c}. \tag{5.24}$$

Eq. (5.24) is identical to Eq. (5.19), which means that the Fourier variable associated with the slow-time τ is the Doppler frequency.

A radar is said to be coherent if it preserves the phase history of the targets (see Eq. 5.21). If the radar is coherent, then the obtaining of the Doppler becomes trivial, after applying a Fourier transform (i.e., an FFT) to the slow-time signal. If a time-frequency transform (such as the spectrogram or the Wigner−Ville distribution) is applied to this signal, the Doppler frequency as a function of the slow-time τ (i.e., the Doppler history of the targets) can be reconstructed. An incoherent radar can only obtain range profiles and its performance is always poorer than that of a coherent radar [31]. The LFMCW radars here exposed are coherent. To preserve the phase information, a careful design of the radar becomes mandatory. As stated later, the most important rule is that the generation and acquisition blocks share the same clock [25].

Regarding the coherence preservation at the Tx part, the arrows shown in Fig. 5.5 highlight the initial phase for each transmitted waveform period. These initial phases must be equal (or at least known, to compensate for their effects). The generation block (normally based on DDS and voltage-controlled oscillator technologies) is normally capable of guaranteeing this phase control. Depending on the particular design, the irrelevant unprocessed interval T_r shown in Fig. 5.5 can be useful to match the aforementioned phases, since it can make easier the solution to possibly-arising locking-related issues.

More importantly, the generation and acquisition blocks must share a common clock or, at least, the clock shifts must be known. In other words, the samples taken by the ADC must be synchronized with the produced ramps in order to
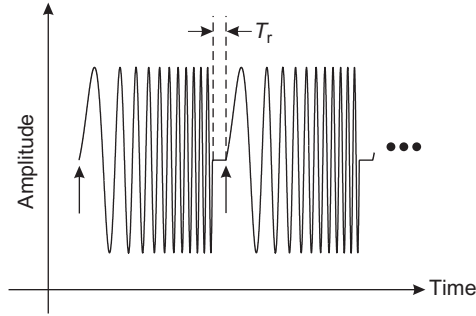
FIGURE 5.5

Control of the initial phase for each transmitted ramp to guarantee radar coherence.

guarantee that no additional unknown phase term is added to Eq. (5.21). If this synchronization is achieved, the number of samples of the beat signal for each waveform period T is constant.

The lack of clock-matching can mean a severe degradation for the radar coherence. For example, if the unwanted additional phase term in Eq. (5.21) is a white uniform stochastic process between $-\pi$ and π, the phase history of the target is completely destroyed and no Doppler reconstruction is possible. In practice, these things are not so bad, and the fact of using different clocks at the generation and acquisition stages leads to a slow phase-drifting, which is typically observed as a quasi-linear leaning of the always-present zero-Doppler returns. In that case, the data formatting becomes, however, uncomfortable, since the number of samples of the beat signal per each period T is not constant.

5.3.3 OBTAINING OF THE RANGE

Human-aware localization is a short-range application. Depending on the specific scenario, different information can be interesting to be extracted. For example, if the application consists in the detection of people trapped after a snow avalanche, the vital signs can be used as moving targets. In a healthcare scenario, an exact monitoring of the respiration and/or heartbeats can be of high interest. For gaming applications, it may be useful to analyze the human gait and monitor the different parts of the body (hands, arms, legs, etc.), which have different range histories, referred to as micro-Doppler signatures [42].

A common denominator for all these human-aware applications is the interest in obtaining the range histories (or, equivalently, Doppler histories) of different scatterers, while trying to avoid interferences among them. A short-range coherent LFMCW radar sensor is often preferred for this task and, furthermore, provides range resolution which can be very useful for the isolation of individual scatterers.

Eq. (5.14) gives the key to derive two independent algorithms to extract the range history $R(\tau)$ of the illuminated point-scatterer target:

- An amplitude-based tracking of the range, which uses the sinc factor of Eq. (5.14).
- A phase-based tracking of the range, which uses the exponential factor of Eq. (5.14).

In relation to the amplitude-based algorithm, the idea consists in tracking the amplitude peak from range profile to range profile. As will be seen later in Section 5.5.2, this algorithm is not very precise and usually suffers from the target-scintillation phenomenon. In practice, any target must be considered as the combination of many little scatterers, so that the received signal is the coherent sum of many single contributions. Little changes in the aspect angle of the target lead to amplitude fluctuations, which make the range profile have a noisy appearance, even when the SNR is high [30,31].

In relation to the phase-based algorithm, the range can be extracted by making use of Eq. (5.21). That is, the range $R(\tau)$ can be written as [25]

$$R(\tau) = \frac{c \cdot \phi_{\mathrm{t}}(\tau)}{4\pi f_{\mathrm{c}}}. \tag{5.25}$$

This algorithm must first extract the phase history of the desired target. To that purpose, it is clear that (1) the radar must be coherent, and (2) the desired phase $\varphi_{\mathrm{t}}(\tau)$ must be isolated from surrounding powerful interferences (these unwanted targets are usually referred to as clutter). Details will be given later in this chapter.

Additionally, the phase history $\varphi_{\mathrm{t}}(\tau)$ must be unwrapped, because the measured phase always takes values between $-\pi$ and π. The phase-unwrapping algorithm works in a one-dimensional space, and thus it is usually simple, especially when the phase jump between any two consecutive slow-time instants is not greater than 2π. This implies that the along-LOS range motion of the target should not exceed $\lambda/2$ between any two consecutive periods. In practice, and especially for the slow targets here referred to, this limit is not overcome and the phase-based algorithm can be easily implemented.

The phase-based algorithm to extract the range history of scatterers has a better performance in terms of precision in comparison with the amplitude-based algorithm (see Section 5.5.2). Furthermore, it is more robust to the target-scintillation phenomenon.

5.4 SIGNAL PROCESSING ISSUES

The previous section provides the mathematics to understand important concepts around coherent LFMCW radars (such as fast-time, slow-time, range profile, beat signal, Doppler frequency, or range resolution), and the ideas for some algorithms. This section makes use of the previous results to justify the standard

signal processing manipulations usually made for coherent LFMCW radar sensors. Aspects about data formatting, construction of important matrices, and algorithms for range tracking of targets are provided.

5.4.1 DATA FORMATTING

Fig. 5.2 indicates that the signal to be sampled is the beat signal, which is obtained after the mixing of the returned echoes with a replica of the transmitted signal (deramping technique). The conventional data formatting for a coherent LFMCW radar is shown in Fig. 5.6. As seen, the beat signal is sampled at the rate of the low-end ADC (sampling frequency f_s) during a long period of time (say some seconds). For a coherent radar, the total time to be sampled is referred to as the coherent processing interval (CPI).

After the acquisition of the beat signal during the total time CPI, a large number of samples is available (N_{CPI}). The usual data formatting consists in stacking the samples of the beat signal in rows of the so-called "raw-data matrix," so that the horizontal dimension of the matrix (along columns) is the fast-time. The number of samples in each row N corresponds to one waveform period T, and can be mathematically written as

$$N = \lfloor f_s \cdot T \rfloor \tag{5.26}$$

where the function $\lfloor x \rfloor$ refers to the lowest integer of x.

The vertical dimension of the raw-data matrix (along the rows) corresponds to the slow-time τ. The number of rows M (i.e., the number of slow-time instants) is given by

$$M = \left\lfloor \frac{CPI}{T} \right\rfloor = \frac{N_{CPI}}{N}. \tag{5.27}$$

Only a perfect coherence of the radar guarantees that the number of samples per row is constant with the time. The raw-data matrix clearly puts emphasis on the fact that the sampling frequency corresponding to the fast-time t is the
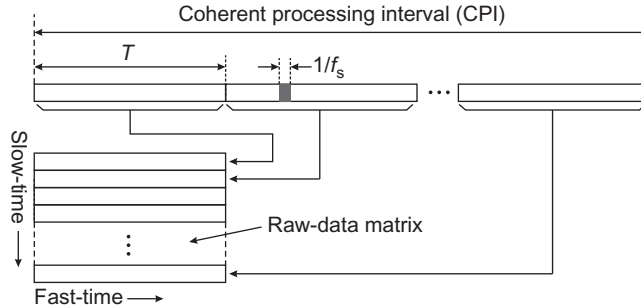

FIGURE 5.6

Conventional data formatting for a deramping-based coherent LFMCW radar.

sampling frequency of the ADC f_s, whereas the sampling frequency associated with the slow-time τ is the PRF.

5.4.2 CONSTRUCTION OF IMPORTANT MATRICES

The raw-data matrix contains the samples directly obtained by the ADC. Assuming an I/Q demodulation, the elements of the matrix are complex-valued. Obviously, the raw-data matrix contains contributions from the desired targets, thermal noise of the receiver, clutter (undesired targets), hardware mismatches, spurious signals, interferences, and so forth [30,31].

Given these $M \times N$ complex values, signal processing manipulations (i.e., algorithms) are required for multiple purposes, such as detection based on thresholding, target localization, construction of tracks based on a Kalman filtering, imaging, etc. For a short-range LFMCW radar and human-aware localization applications, the most interesting output of the intended algorithms is the range history of some scatterers, as previously mentioned. In this context, the reader must be familiar with the three following matrices in the context of a coherent LFMCW radar:

- The raw-data matrix $\mathbf{M}_r$.
- The range-profile matrix $\mathbf{M}_{rp}$.
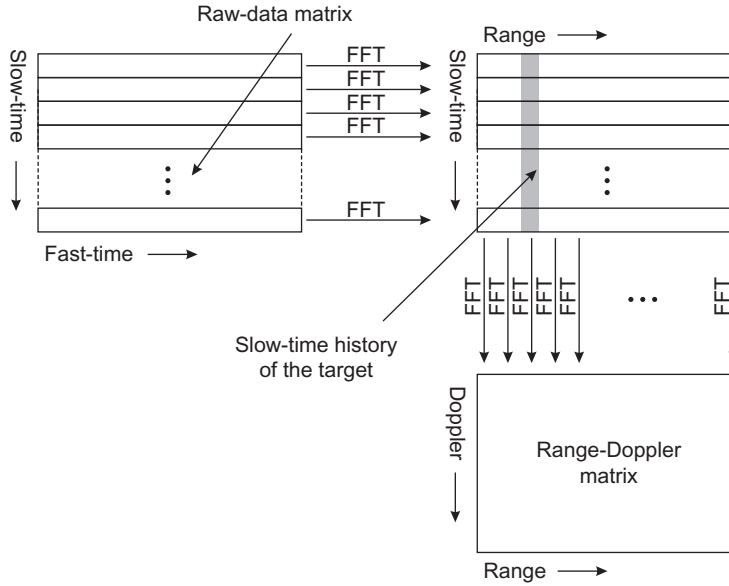- The range-Doppler matrix $\mathbf{M}_{r,Dop}$.

The previous section has profoundly explained the raw-data matrix. Regarding the range-profile matrix, one should note that a Fourier transform for each row of the raw-data matrix gives rise to it, since the beat frequency is proportional to the range for deramping-based LFMCW radars (see Section 5.3). Fig. 5.7 schematically shows the obtaining of this range-slow-time matrix $\mathbf{M}_{rp}$ (i.e., the range profiles) from the original raw-data matrix.

After noting that the Doppler is the frequency associated with the slow-time τ (see Section 5.3), it becomes trivial that a column-wise Fourier transform of the range-profile matrix leads to obtaining the range-Doppler matrix $\mathbf{M}_{r,Dop}$ (see Fig. 5.7). Since the slow-time is sampled at the PRF rate, it comes to light that the unambiguous interval for the Doppler is $[-PRF/2, PRF/2]$, which means an unambiguous interval from $-\lambda \cdot PRF/4$ to $\lambda \cdot PRF/4$ for the radial along-LOS velocity of the targets.

The range-Doppler matrix is usually referred to as the inverse synthetic aperture radar (ISAR) image, since in ISAR the cross-range is proportional to the Doppler and thus, a scaled projection of the target shape may be reconstructed (in range and cross-range dimensions) [33].

5.4.3 ALGORITHMS TO EXTRACT THE RANGE HISTORY

Section 5.3.3 anticipated two algorithms to extract the range history of target scatterers. Their advantages and drawbacks were also given in Section 5.3.3. Here,

Raw-data matrix

Range ⟶

Slow-time

Fast-time ⟶

FFT
FFT
FFT
FFT

FFT

Slow-time

Slow-time history
of the target

FFT FFT FFT FFT FFT   • • •   FFT

Doppler ⟶

Range-Doppler
matrix

Range ⟶

FIGURE 5.7

Construction of the range-profile and range-Doppler matrices from the raw-data matrix.

the algorithms are described under the signal processing framework of this section. Note that the information here provided is complementary to Section 5.6, where some ideas about clutter mitigation can lead to a better range tracking of short-range scatterers.

Assume that the raw-data matrix is called $\mathbf{M}_r[m, n]$ ($m = 1, 2, \ldots, M$; $n = 1, 2, \ldots, N$). M is the number of rows of the matrix (i.e., the number of transmitted ramps) and N is the number of samples for each waveform period T (i.e., the number of columns).

5.4.3.1 Amplitude-based algorithm

This algorithm to extract the range history of a target can be used with an incoherent radar, with the penalty of a reduced performance. The idea is simple: one must track the peak corresponding to the target in order to derive the range history. Moreover, to attain better precision in the determination of the peak position, the technique of "zero-padding" is conventionally employed. The details of the amplitude-based algorithm are given next:

- Apply an FFT of N_{FFT} points to each row of the matrix $\mathbf{M}_r[m, n]$. N_{FFT} is much larger than N. The resulting matrix is the range-profile matrix $\mathbf{M}_{rp}[m, k]$, where $k = 0, 1, \ldots, N_{FFT} - 1$.
- For each range profile m, obtain the value of k for which the magnitude of the range profile is maximum. Call to this value $k^*[m]$.

• Obtain the range evolution of the target as Eq. (5.28) indicates.

$$R(\tau) = k^*[m] \frac{f_s}{N_{FFT}} \cdot \frac{c}{2\gamma}. \tag{5.28}$$

The proposed method utilizes an interpolation to gain some precision in the determination of the peak position. Normally, large values of N_{FFT} are required, which leads to a computationally-costly Fourier transform. Simpler algorithms can use a parabolic interpolation only based on the neighboring samples surrounding the peak [30]. In any case, this method has a performance poorer than the phase-based algorithm and is less robust to the target-scintillation phenomenon.

5.4.3.2 Phase-based algorithm

If the coherence is properly preserved, this algorithm can be applied. Basically, it adapts the data to extract the slow-time phase history of the desired target, which is assumed to be situated in the same range bin during all the CPI (i.e., there is no range migration of the target). The range evolution can then be extracted from the unwrapped phase history, as suggested by Eq. (5.25).

The phase-based algorithm to extract the range history is divided into the following steps [25]:

• Apply an FFT to each row of the matrix $\mathbf{M}_r[m, n]$. The resulting matrix is the range-profile matrix $\mathbf{M}_{rp}[m, n]$.
• Select the range bin n^* within which the target is contained. Pick up the corresponding column of $\mathbf{M}_{rp}[m, n]$ to construct the signal $s[m] = \mathbf{M}_{rp}[m, n^*]$.
• Obtain the phase of the signal $s[m]$ and proceed with its unwrapping.
• Apply Eq. (5.25) to derive the range evolution of the target.

As previously commented, the phase unwrapping should not be problematic. Also, if there is migration of the target through range cells during the CPI, specific algorithms (such as the extended envelope correlation or global range alignment) can be applied without affecting the desired phase history [40,41].

5.5 RANGE RESOLUTION, PRECISION, AND ACCURACY

An important measure of radars is the range (i.e., the along-LOS distance to the target). Moreover, the determination of the range history of scatterers is here identified as the key output product for short-range human-aware localization applications. Two algorithms to derive the track history of targets have been provided in Section 5.4.3. In this section, a big emphasis is put on the concepts of range resolution, precision, and accuracy [30−33], which are sometimes used confusedly in the literature. A brief subsection addresses the same concepts for other dimensions.

5.5.1 **RANGE RESOLUTION**

The range resolution of a radar refers to its ability to discriminate (i.e., to resolve) two close targets in range. Assuming a 3-dB criterion and a uniform weighting (i.e., a uniform window), the range resolution of a radar has the general expression [30−33]

$$\Delta R = \frac{c}{2B},$$

(5.29)

where c is the speed of light, and B is the instantaneous transmitted bandwidth.

Eq. (5.29) is valid for an LFMCW radar, as demonstrated in Eq. (5.17), and is intimately connected with the fundamental limit of the Heisenberg's uncertainty principle (in the signal processing area, this limitation is usually addressed as the Gabor limit).

According to Eq. (5.29), if one looks for an improvement in the range resolution, the only way to achieve it is to transmit and to handle a larger bandwidth B. If the transmitted bandwidth is very large, one real target may be viewed as an extended target (i.e., the LOS dimension of the target is chopped in many pieces). If one does not have hardware and/or budget limitations, a finer range resolution is always pursued, because richer information (e.g., more interesting radar signatures) from the target can be extracted.

There are some techniques (such as MUSIC, Capon estimator, Autoregressive coefficients, and so forth), usually referred to as superresolution techniques, which can improve the conventional resolution. They are based on parametric models, which assume very specific forms for the signals. Indeed, they work properly for such signals, but can lead to important problems for real signals, such as the appearance of ghost targets and/or the distortion of the Fourier-based radar signatures of targets [43]. In the opinion of the authors, these techniques are controversial. Hence, any reference to resolution in this chapter must be understood as the conventional Heisenberg-limited resolution.

Fig. 5.8 shows the range profile corresponding to two simulated equal-amplitude point scatterers separated 50 cm in range, when illuminated by an LFMCW radar. The range resolution is 15 cm ($B = 1$ GHz), and consequently, the two targets can be easily discriminated. The windowing is uniform, which implies that the secondary lobes appear 13.5 dB below the main lobes. As is widely known, the application of a specific window (e.g., Taylor or Hamming) leads to an increase of the sidelobe rejection, but at the cost of a slight broadening of the main lobe.

When the two targets are very close, it is difficult to tell whether there are two point scatterers or only one. Fig. 5.8 also shows the range profile when the targets are spaced 15 cm (i.e., the range-resolution value). Two little peaks indicate the presence of the two targets. However, the addition of the always-existing noise or an approaching of the two targets would merge them into a single one.

The formula Eq. (5.29) for the range resolution must not be understood as a strong limit for the ability of discriminating two point scatterers. Indeed, depending on the relative phases of the two targets, the two peaks in Fig. 5.8 can be
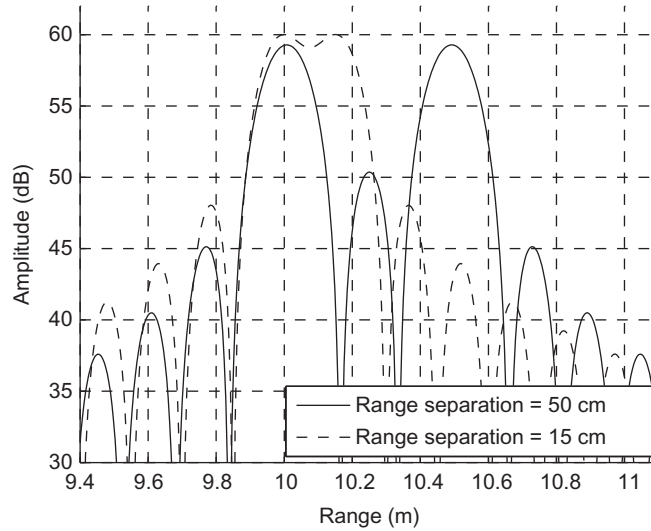
FIGURE 5.8

Range profiles corresponding to two point scatterers spaced 50 cm (continuous line) and 15 cm (dashed line) along LOS.

distinguished more easily. Eq. (5.29) speaks about the broadening of the target PSF and is perhaps the most famous formula for the radar community.

Additionally, the range resolution indicates the range size of the bins/cells of any radar. For example, for a conventional radar plan position indicator, the cells are angular sectors, in which the along-LOS width is given by the range resolution, and the azimuth width mainly depends on the antenna beamwidth.

5.5.2 RANGE PRECISION

When a radar is measuring the range of a point-scatterer target, it obtains an estimate $\hat{R}$. Obviously, the radar will not obtain an exact measurement of the actual range R. There is an error, which can be written as

$$\varepsilon_R = R - \hat{R}. \tag{5.30}$$

The estimate $\hat{R}$ is a function of the observations and thus, it is a random variable. Consequently, the error ε_R is also a random variable, whose probability density function may be very complex, depending on the nature of the observations (e.g., the observations can be the combination of the returns of a fluctuating target, complex clutter, and flicker and thermal noise).

The range precision is defined as the standard deviation of the error ε_R. Anytime that the experiment is repeated, the radar obtains a different value (i.e., a
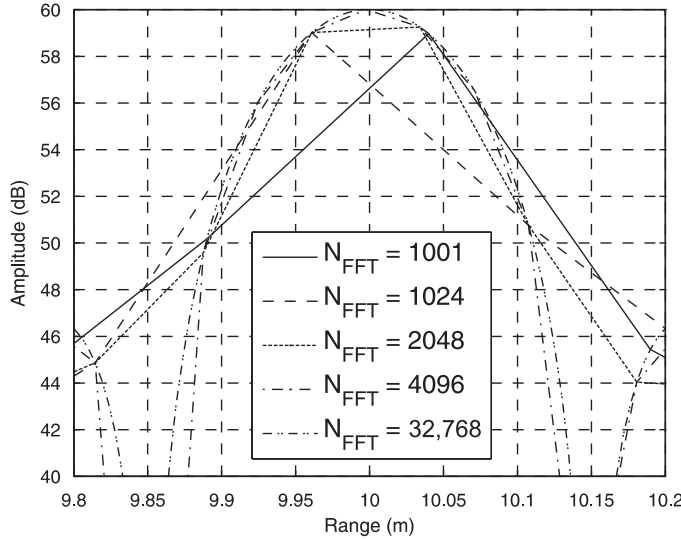
FIGURE 5.9

Range profiles corresponding to a point scatterer for different zero-padding levels.

different realization) for the range estimate. This fluctuating error around the ground-truth value is related to the range precision.

Fig. 5.9 plots the simulated range profile for a point scatterer situated at 10 m from the deramping-based LFMCW radar. The range resolution is $\Delta R = 15$ cm ($B = 1$ GHz), the central frequency is $f_c = 10$ GHz, the period is $T = 1$ ms, and the employed sampling frequency is $f_s = 1$ MHz. The different curves correspond to different points of the FFT (N_{FFT}) in the zero-padding technique (see Section 5.4.3).

As observed, an increase in the N_{FFT} parameter leads to a better estimation of the range position of the point-scatterer target. This is commented in Section 5.4.3 for the amplitude-based algorithm. Table 5.1 details the error as a function of N_{FFT} and confirms the previous asseveration. It comes to light that the amplitude-based algorithm can be very precise (i.e., the error can be very small) for a very high SNR and a nonfluctuating target.

Unfortunately, noise is always present and degrades the precision of any radar. It can be shown that the range precision σ_R of a radar is inversely proportional to the square root of the SNR (the noise is assumed to be white and Gaussian) [30]:

$$\sigma_R = \frac{K}{\sqrt{SNR}}. \tag{5.31}$$

Fig. 5.10 depicts three range profiles for three different realizations and a high number of FFT points ($N_{FFT} = 32768$). The SNR in the beat-frequency domain is considered to be 10 dB. As can be seen, the peak fluctuates around the ground-truth value of 10 m.

Table 5.1 Absolute and Relative Error in the Amplitude-Based Range Measurement of a Simulated Point Scatterer as a Function of the Zero-Padding Level

N_{FFT}	Range of Peak (m)	Absolute Error (cm)	Relative Error (%)
1001	10.04	4	0.4
1024	9.9609	−3.91	−0.391
2048	10.0342	3.42	0.342
4096	9.9976	−0.24	−0.024
32768	10.0021	0.21	0.021
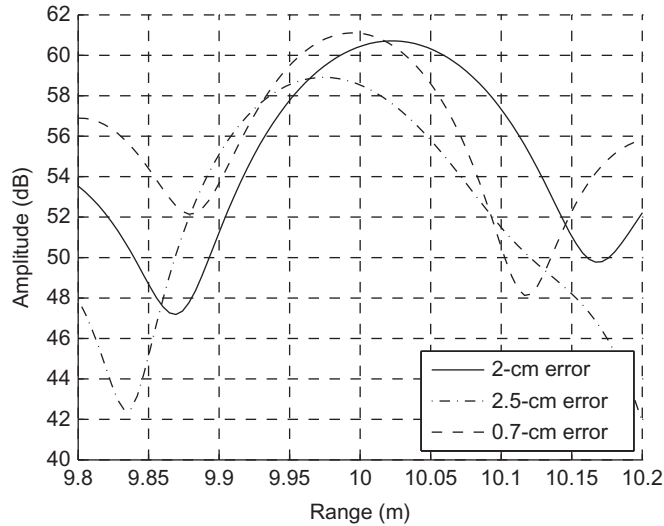
FIGURE 5.10

Realizations of range profiles corresponding to a point scatterer for a SNR of 10 dB.

It is important to highlight the big differences between the concepts of range resolution and precision. The range resolution is related to the width of the target PSF and the ability to discriminate two targets closely spaced in range, whereas the range precision is related to the process of measuring the distance and the associated fluctuating errors.

Regarding the two algorithms provided in Section 5.4.3, both of them have the purpose of estimating the range history of targets. However, their performance is quite different. It can be shown that the range precision for the amplitude-based algorithm is given by [30]

$$\sigma_{R,\text{amp}} = K_1 \frac{\Delta R}{\sqrt{\text{SNR}}}, \tag{5.32}$$

whereas the corresponding equation for the phase-based algorithm can be written as [44]

$$\sigma_{R,\text{phase}} = K_2 \frac{\lambda}{\sqrt{\text{SNR}}}. \tag{5.33}$$

In Eqs. (5.32) and (5.33), the constants K_1 and K_2 are similar. It comes to light that the range precision is usually better for the phase-based algorithm, especially for high-frequency radars. Furthermore, the phase-based method is more robust against the target-scintillation phenomenon, as verified in Section 5.7.4. These advantages for the phase-based method are gained from the effort of constructing a coherent radar.

5.5.3 RANGE ACCURACY

The range precision is related to the standard deviation of the error in Eq. (5.30). The range accuracy refers to the mean (i.e., the expected value) of the error in Eq. (5.30). In other words, it is said that the range measurement is accurate if the range estimate $\hat{R}$ has a small bias [30]. The expected value of $\hat{R}$ can be generally written as

$$E[\hat{R}] = R + R_{\text{bias}} \tag{5.34}$$

where $E[x]$ is the expectation operator for the random variable x, and R_{bias} is the range bias from the ground-truth range R.

The bias observed in a measure is also referred to as a systematic error, since it is repeated every time the same experiment is conducted. Contrary to the range precision, the range accuracy is not related to fluctuating errors, but to a systematic error.

Possible causes for systematic errors can be very complex and even difficult to detect. In an LFMCW radar, one typical origin for a range bias is an uncertainty in the delay of the replica of the transmitted signal at the input of the deramping mixer. In this case, a simple shifting of the range axis can be enough to improve the accuracy of the radar.

The procedures to reduce systematic errors are called calibration processes, which can be very simple (such as the aforementioned shifting of the range axis) or very sophisticated. For example, the multipath phenomenon and/or hardware mismatches can lead to large range biases (or even to ghost echoes).

In any case, it is sometimes difficult to tell in practice (in specific real experiments) whether the measurements are accurate or not. The point is that to calculate the bias R_{bias}, it is necessary to know the ground-truth range R (see Eq. 5.34). This range R has been defined for a point-scatterer target, which is not a real entity. Real targets are always extended targets, for which it is difficult to tell their real and single range R. For example, a metal plate illuminated by a radar can have returns from its surface and from its edges, but the radar singly observes the coherent combination of all these returns.

This leads to the fact that little variations on the experiment configuration may require different calibration procedures. There are sometimes additional available measurements (e.g., an infrared marker to monitor vital signs) and, of course, calibration procedures could be applied to match the radar measures to the available ones. In any case, these reference measures are not necessarily identical to the ground truth.

The tolerance to systematic errors largely depends on the specific application, and normally, the calibration procedures are designed to be simple. All in all, the important aspect is to note that the range accuracy is different from the range precision and that a better SNR does not necessarily imply having a more accurate radar sensor.

5.5.4 OTHER DIMENSIONS

The concepts of resolution, precision, and accuracy can be applied to other dimensions beyond the aforementioned range. In the case of radar systems, the Doppler and the angle (e.g., azimuth and elevation) are to be considered.

In relation to the Doppler frequency, a good Doppler precision requires a high SNR, whereas systematic Doppler errors require calibration procedures [30,33]. On the other hand, a good Doppler resolution requires a large CPI, but note that target scatterers usually change their Doppler frequencies during long times. In ISAR contexts, big efforts are devoted to compensating for the motion of the targets [33].

Regarding the angle, a good angular precision again requires a high SNR, and calibration may be required to improve the angular accuracy. Different techniques to precisely mark the azimuth/elevation of the targets have been proposed, such as the well-known monopulse technique or the moving-window technique. On the other hand, the angular resolution is limited by the beamwidth of the radar antenna. Hence, if a better angular resolution is desired, a larger antenna, a phased array, or a synthetic array (e.g., SAR techniques) may be used [30,33].

5.6 CLUTTER MITIGATION

In a general sense, clutter is any returned echo which affects the correct estimation of the parameters of wanted targets. For human-aware localization scenarios, the desired output has been here identified as the range history of the target scatterers. Any clutter return which may have an influence on the correct extraction of this range history should be sought to be mitigated.

LFMCW radars have range resolution, and thus it becomes trivial that clutter returns in range bins different from the range cell in which the desired target is located will not have a big influence on the correct estimation of the range history of the target (note that problematic secondary lobes of clutter may be mitigated

by simple windowing). This clutter-isolation property is a clear advantage for LFMCW radars in comparison with conventional Doppler radars, which do not transmit an instantaneous bandwidth. An incoherent LFMCW radar can also exploit this clutter-isolation property [45−47].

A more complex scenario is the one in which the clutter returns are located at the same range bin of the wanted target. For example, in a vital sign monitoring scenario, the stationary limbs of the breathing subject (e.g., the legs and the arms) may influence the correct range tracking of respiration and heartbeats [45−47].

If the clutter echoes are situated at the same range cell of the wanted target (and, of course, both of them are within the radar antenna beamwidth), and the radar is incoherent, the only difference between them is the amplitude of the corresponding signals. Only if the signal-to-clutter ratio (SCR) is high, a correct tracking of the wanted range history will be possible. On the contrary, if the radar is coherent, the Doppler domain is available to try to filter/mitigate the clutter echoes.

This clutter filtering will be effective if the Doppler signatures of the clutter and the target can be distinguished. In other words, if the Doppler-domain spectrums of clutter and target are quite different, the application of a suitable filter may mitigate the degrading effects of clutter. In the case of the vital sign monitoring application, the implied signals (i.e., respiration and heartbeats) are very slow and weak, so that the mitigation of the stationary clutter (e.g., legs, arms, and head) becomes very challenging. In the case that the clutter is powerful and moving (e.g., when trying to monitor the vital signs of a sleeping patient who is moving in the bed), the radar-based noncontact tracking of the respiration and heartbeats becomes almost an impossibility.

The next subsections provide the mathematics and algorithms to understand the ideas underlying the Doppler-based clutter-mitigation methods for a coherent LFMCW radar. The application of the methods to simulated and experimental data is provided in Sections 5.7.5 and 5.8.3.

5.6.1 MATHEMATICAL FORMULATION

From Section 5.4, and assuming that there are no range migrations, it comes to light that the slow-time signal for the range bin in which the target is located (deramping-based coherent LFMCW radar) can be written as [46]

$$s(\tau) = K \cdot \exp\left(j\frac{4\pi f_c}{c} R(\tau)\right) \qquad (5.35)$$

where K is the amplitude of the desired signal, and $R(\tau)$ is the wanted range history. From Eq. (5.35) and also according to Eq. (5.21), the phase history for the desired target is given by

$$\phi_d(\tau) = \frac{4\pi f_c}{c} R(\tau). \qquad (5.36)$$

Suppose the existence of a stationary point-scatterer clutter echo situated at the same range bin. The clutter-plus-target signal in that range bin can be expressed as

$$s_r(\tau) = K_d \cdot \exp(j\phi_d) + K_c \cdot \exp(j\phi_c) \tag{5.37}$$

where K_d and φ_d are the amplitude and phase of the desired target (see Eq. 5.36), whereas K_c and φ_c are the amplitude and phase of the clutter scatterer, respectively. The clutter phase φ_c can be written as

$$\phi_c = \frac{4\pi f_c}{c} R_c \tag{5.38}$$

where R_c is the range of the clutter scatterer. Note that the clutter phase Eq. (5.38) is constant with the slow-time τ, since the clutter scatterer has been assumed to be stationary.

By noting Eq. (5.37), the SCR is defined as

$$SCR = \frac{|K_d|^2}{|K_c|^2}. \tag{5.39}$$

For the particular case of a low SCR (SCR $<<$ 1), Fig. 5.11 schematically shows the complex phasor representation of Eq. (5.37).

Geometrical observations in Fig. 5.11 permit the conclusion that the slow-time signal Eq. (5.37) can be written as follows for a low SCR

$$s_r(\tau) = K_r \cdot \exp(j\phi_r) \tag{5.40}$$

where K_r is approximately equal to K_c, and the phase φ_r must fulfill the following equation:

$$\tan(\phi_r - \phi_c) = \frac{K_d \sin(\phi_d - \phi_c)}{K_c + K_d \cos(\phi_d - \phi_c)}. \tag{5.41}$$

For a low SCR, note that

$$\tan(\phi_r - \phi_c) \approx \phi_r - \phi_c, \tag{5.42}$$
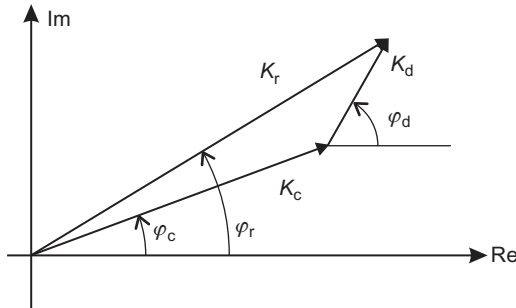
FIGURE 5.11

Complex phasor representation of the slow-time signal in Eq. (5.37) for a low SCR.

$$K_c >> K_d \cos(\phi_d - \phi_c), \tag{5.43}$$

which leads to the fact that the phase extracted by the phase-based algorithm in Section 5.4.3 would be [46]

$$\phi_{r,\ \text{low SCR}} = \phi_c + \frac{K_d \sin(\phi_d - \phi_c)}{K_c}. \tag{5.44}$$

As concluded from Eq. (5.44) and after noting that $K_c >> K_d$ (SCR $<< 1$), the reconstructed phase φ_r is almost identical to the clutter phase φ_c, and no information from the desired phase can be recovered. This necessitates a clutter-mitigation technique.

On contrary, the phase φ_r for a high SCR can simply be written as [46]

$$\phi_{r,\ \text{high SCR}} = \phi_d + \frac{K_c \sin(\phi_c - \phi_d)}{K_d}. \tag{5.45}$$

In the case of a high SCR, the reconstructed phase is nearly the desired one. Nevertheless, the second term in Eq. (5.45) indicates that clutter can have some influence on the exact extraction of the wanted range history even for a high SCR.

5.6.2 DOPPLER-BASED CLUTTER MITIGATION

Depending on the relative level of the clutter return and the desired target, the previous section has demonstrated that clutter can completely obscure the wanted range history of the target. A HRR is always preferred, because it confers range-isolation capabilities upon the radar system. However, it is sometimes unavoidable to have clutter returns at the same range bin of the desired target. If the radar is coherent, a Doppler-based filtering can still alleviate the effects of the clutter [45−47].

As demonstrated in Section 5.3.2, the Fourier variable associated with the slow-time τ is the Doppler frequency, and hence the PRF is the sampling frequency for these slow-time signals, such as the one in Eq. (5.37). The second term of Eq. (5.37) corresponds to a stationary-assumed clutter scatterer, which means a zero-Doppler component; whereas the first summand refers to the moving target and gives rise to a broader lowpass Doppler spectrum. For example, if the desired range is assumed to vary sinusoidally (e.g., a respiration signal may be modeled as a tone), the Doppler spectrum for the vital sign is the well-known spectrum of a signal frequency-modulated by a modulating sinusoid—i.e., some Bessel-weighted deltas separated by the sinusoid frequency with an overall bandwidth estimated by Carson's rule.

Thus, for a coherent radar, clutter appears as a zero-Doppler component, and the desired target has a broader low-pass-type spectrum. Fig. 5.12 schematically emphasizes these features. As observed, overlapping of both signal spectrums is a fact. However, the clutter can be mitigated if a high-pass digital filter is applied
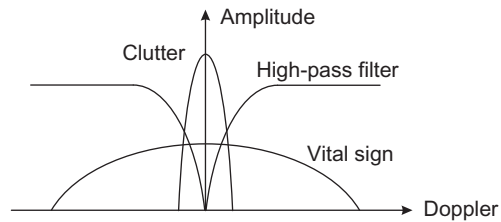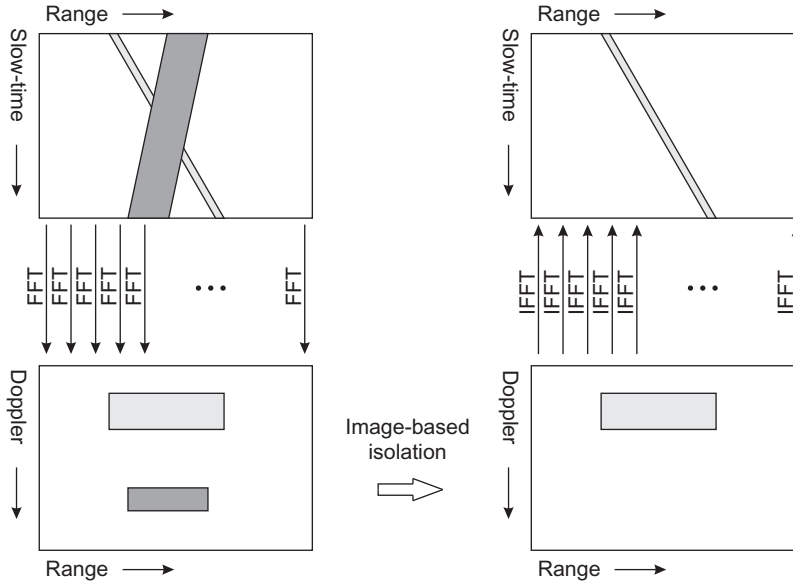
FIGURE 5.12

Schematic plotting of the Doppler spectrums corresponding to a stationary clutter echo and a slow-moving target.

to the slow-time signal. Conventional coherent surveillance radars use these filters (usually called cancelers) to reduce the levels of surface clutter (e.g., land and crops) [30–31]. The technique extrapolated here to short-range radars belongs to the so-called MTI Doppler-mitigation approaches. However, the differences between both scenarios are big, because for human-aware localization applications and especially for vital-sign monitoring, the implied signals are very slow and the bandwidth of the desired spectrum is usually small.

The suggested high-pass filter in Fig. 5.12 attenuates the very low-frequency Doppler components of the wanted slow-time signal. Consequently, the distortion on the desired signal is inevitable. The design of the high-pass digital system must search for a tradeoff between a proper mitigation of the clutter and a tolerable distortion of the extracted range evolution of the desired target. Examples will be given in Section 5.7.

In conclusion, when having a coherent radar, it is always mandatory to take a look at the possibilities of exploiting the Doppler dimension to mitigate clutter. For example, in a gaming scenario where some people are moving in a room, it may be interesting to isolate the range tracks of each person. Fig. 5.13 schematically shows a processing to isolate the range histories of two people (one moving away from the radar and the other approaching the radar). Fig. 5.13 (top left) shows the range-profile matrix, where two leaned echoes can be seen. After applying an FFT in the slow-time dimension, two returns from the two people are isolated in the range-Doppler domain (Fig. 5.13 (bottom left)). An image-processing windowing (or clustering) can be used to isolate one of the returns, as Fig. 5.13 (bottom right) shows for the receding person. An inverse FFT (IFFT) returns the isolated echo to the range-slow-time domain (Fig. 5.13 (top right)). In this domain, a range-bin-alignment method together with the phase-based algorithm of Section 5.4.3 can be applied to extract the range history of the isolated person.

An important conclusion is that, contrary to incoherent radars, the Doppler dimension can be exploited for clutter-mitigation purposes in coherent short-range deramping-based LFMCW radars.

FIGURE 5.13

Bi-dimensional Doppler-based clutter/interference-mitigation technique.

5.7 SIMULATIONS

In previous sections, many important concepts and algorithms regarding coherent deramping-based LFMCW radars have been introduced. In this section, some simulated results are shown with the aim of emphasizing the main aspects of this kind of radar for short-range human-aware localization applications. The code for the simulations has been developed under the signal processing environment Matlab.

5.7.1 PROOF-OF-CONCEPT SIMULATION

For this first simulation, consider the scenario shown in Fig. 5.14. A coherent LFMCW radar is illuminating a point scatterer situated at a mean range of R_c. The scatterer is sinusoidally vibrating along the LOS. The peak-to-peak motion of the scatterer is given by the parameter R_{pp}, whereas the motion frequency is given by f_t. In this example, R_c is 5.625 m, R_{pp} is 30 cm, and the frequency of the sinusoidal motion is $f_t = 0.5$ Hz.

In relation to the simulation, the important parameters of the radar are summarized as follows. An S-band radar working at $f_c = 5.8$ GHz is assumed. The transmitted bandwidth is 160 MHz, which provides the radar with a range resolution of $\Delta R = 93.75$ cm, according to Eq. (5.17). Given the considered very slow motion (which is typical for human-centered applications), the induced Doppler is
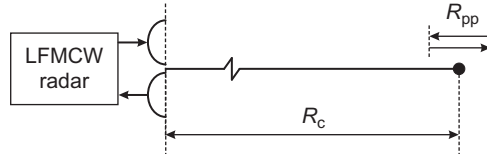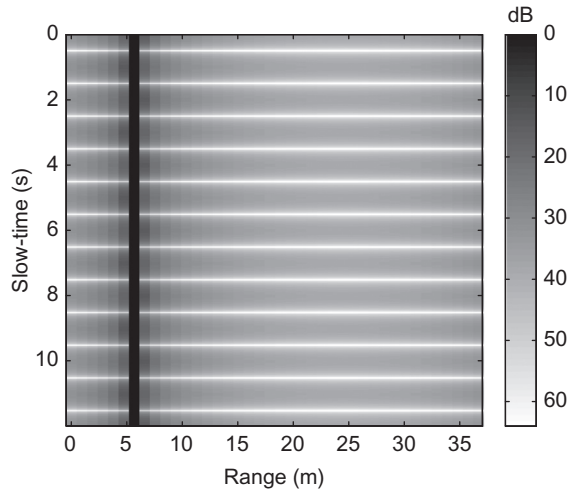
FIGURE 5.14

Simulated scenario for a point-scatterer target sinusoidally vibrating along LOS.

small, and thus the PRF is not chosen to be very high (PRF = 200 Hz). The CPI is 12 seconds, so that it is long enough to observe some periods of the wanted slow signal (the period of the sinusoidal motion is 2 seconds). The sampling frequency in the simulation is assumed to be 8 kHz, which implies a maximum range from which echoes are assumed to come of 37.5 m, according to Eq. (5.12). This low sampling frequency means a simple and inexpensive architecture for the radar prototype. From the simulation viewpoint, a low sampling frequency implies a reduced computational burden, since the number of samples is not very large. Indeed, the number of samples of the beat signal associated with the waveform period T ($T = 5$ ms) is $N = 40$ according to Eq. (5.26), and the number of transmitted ramps is $M = 2400$ (see Eq. 5.27). This means that the raw-data matrix is not very large and has 2400 rows and 40 columns.

Fig. 5.15 shows the range-profile matrix $\mathbf{M}_{rp}[m, n]$, after applying a row-wise FFT to the raw-data matrix (refer to Fig. 5.7). As seen, the target appears situated at the seventh range bin during the CPI, and no range migrations are observed for it, because its sinusoidal motion is not greater than the range resolution $\Delta R = 93.75$ cm (i.e., it is not greater than the range size of the radar cell). The secondary lobes can be observed next to the main vertical strip in Fig. 5.15. Remember that the level of secondary lobes can be reduced through simple weighting (e.g., Hamming or Taylor windowing), at the cost of a width increase of the main lobe.

The result of applying the phase-based algorithm in Section 5.4.3 is shown in Fig. 5.16, which shows the range history extracted for the sinusoidally-moving point-scatterer target. As seen, the range history can be perfectly recovered, since no noise (and thus, an infinite SNR) has been considered in the simulation. Fig. 5.16 also shows that the stage of phase unwrapping is of high importance if a proper tracking of the target motion is desired, because the original phase extracted for the seventh column of the matrix $\mathbf{M}_{rp}[m, n]$ in Fig. 5.15 is wrapped between $-\pi$ and π.

One important point to emphasize is the fact that the range-tracking ability shown in this section is not related to an absolute-range tracking. Indeed, as far as an absolute range marking of the target is concerned, one should simply conclude that the scatterer is situated at the seventh range bin. This is the normal output after the detection stage for a conventional radar: the target is in a specific radar cell/bin. In any case, it is obvious that, depending on the real SNR and the target-scintillation phenomenon, a more-precise measure of the absolute range might be gained after applying, e.g., the amplitude-based method in Section 5.4.3.

FIGURE 5.15

Simulated range-profile matrix for a vibrating scatterer illuminated by an LFMCW radar.
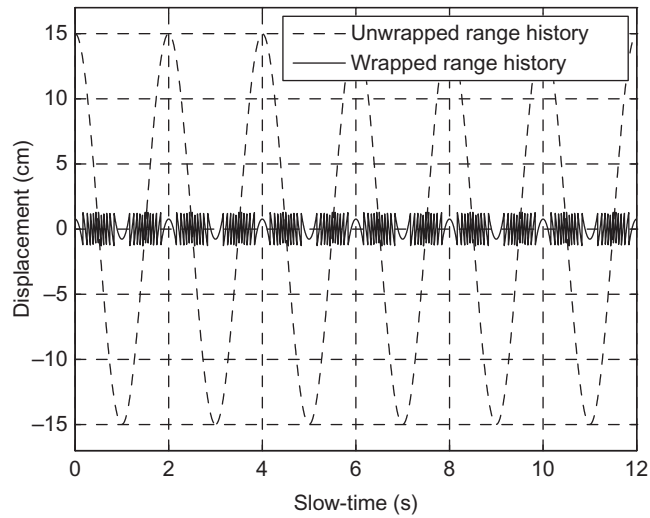
FIGURE 5.16

Wrapped and unwrapped range histories for a vibrating scatterer after applying the phase-based method.

5.7.2 CLUTTER IN OTHER RANGE BINS

Conventional coherent Doppler radars can obtain the range history of the wanted target by making use of the phase-based algorithm. However, these radar sensors do not transmit bandwidth and thus, they do not have range resolution (see Section 5.1). As a consequence, echoes coming from surrounding clutter may have a great influence on the correct derivation of the desired range evolution. Contrary to Doppler radars, LFMCW radars do possess range resolution and hence, they can benefit from this range-isolation capability.

To show this potentiality, a simulation of a wanted scatterer together with a moving clutter return has been conducted. The simulation parameters are the same as those in Section 5.7.1 for the desired point-scatterer target, whereas the unwanted target (clutter) is assumed to uniformly move along LOS from a range of 1 m to a range of 15 m during the 12-second CPI. Fig. 5.17 shows the range-profile matrix (i.e., the range-slow-time map) for this simulation scenario. The wanted target remains in its seventh range bin, whereas the clutter scatterer is subject to a linear motion through resolution cells. The range crossing of both histories happens at around 4 seconds.

Fig. 5.18 shows the result of applying the phase-based algorithm in Section 5.4.3 to the seventh range bin in which the desired target is located. Around the time interval in which the two scatterers are situated at the same range cell, the interference is manifest. At other slow-time intervals, the effect of
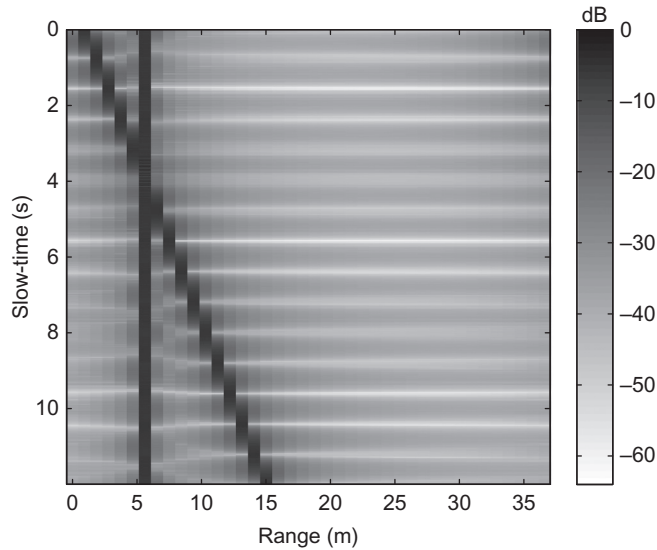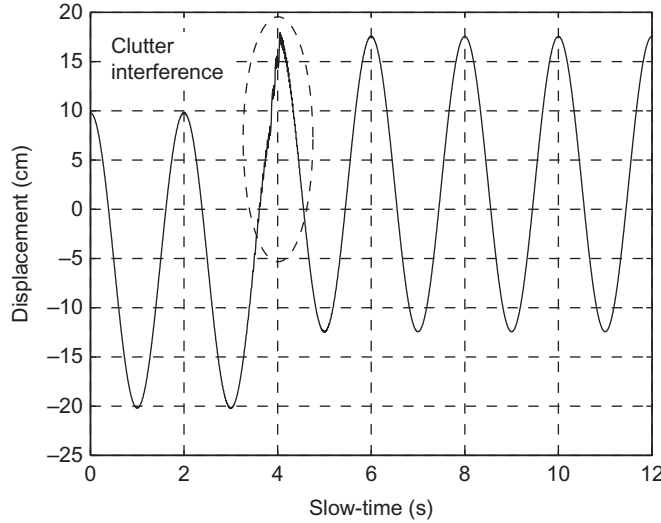

FIGURE 5.17

Simulated range-profile matrix for a desired vibrating point-scatterer target and an unwanted moving clutter scatterer.

FIGURE 5.18

Range history extracted for a desired vibrating scatterer. The clutter influence is manifest.

the clutter scatterer on the desired range history is minor and the correct sinusoidal pattern with the adequate periods and amplitudes can be retrieved.

This section highlights a big advantage of having a good range resolution: clutter returns at other range bins usually have a minor effect on the range tracking of the wanted scatterer. This is contrary to the Doppler radars. In any case, it is clear that clutter returns situated at the desired range bin may have a big influence on the correct results, as seen in Fig. 5.18 and also anticipated in Section 5.6. Results around the application of clutter-mitigation techniques for in-cell clutter are given later.

5.7.3 PERFORMANCE AGAINST NOISE

Fig. 5.16 has shown that an infinite SNR leads to a perfect reconstruction of the range history of the desired point scatterer. It becomes clear that a poorer SNR should mean an imperfect tracking of the range evolution. The mean square error (MSE) is defined as

$$\text{MSE} = \frac{1}{M} \sum_{m=1}^{M} (R_\text{t}[m] - \hat{R}_\text{t}[m])^2 \tag{5.46}$$

where $R_\text{t}[m]$ is the ground-truth slow-time range history of the target, and $\hat{R}_\text{t}[m]$ is its estimate.

Fig. 5.19 shows the MSE as a function of the beat-signal SNR for the scatterer of Section 5.7.1 when centered on the range cell ($R_\text{c} = 5.625$ m) and at a range-bin extreme ($R_\text{c} = 5.15625$ m). The Monte Carlo method is employed so that each
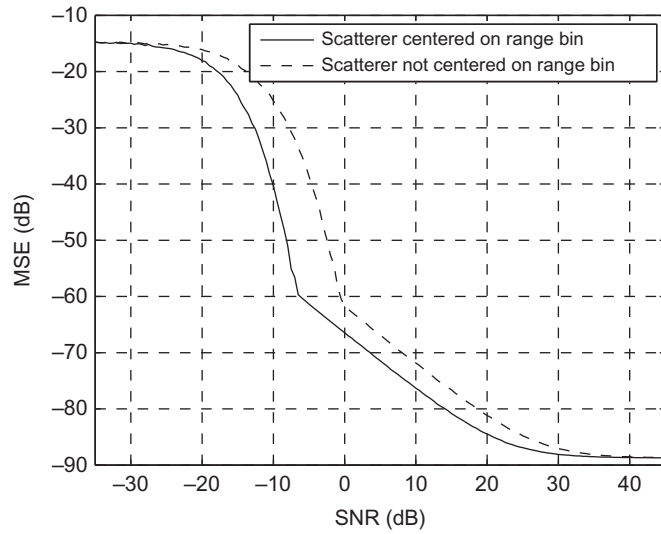
FIGURE 5.19

Performance of the phase-based method against white and Gaussian noise. The MSE is plotted as a function of the SNR.
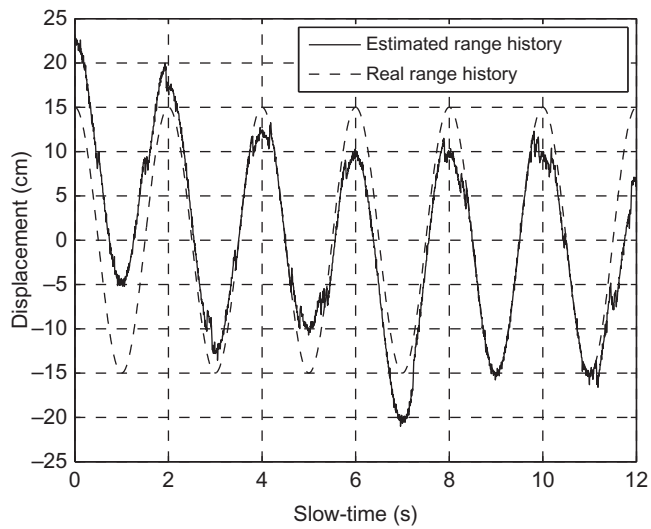
FIGURE 5.20

Estimated range history of a vibrating scatterer for an SNR of −15 dB.

graph point is the average of one thousand realizations, where the noise has been considered to be white and Gaussian. It comes to light that a higher SNR leads to a better reconstruction of the range history in terms of the MSE. The MSE saturation observed for very poor SNRs comes from the fact that the corrupted phase oscillates in the interval $[-\pi, \pi]$, whereas the MSE saturation for high SNRs is explained by numerical negligible errors.

As an example, Fig. 5.20 depicts the range-history reconstruction for one realization with an SNR of -15 dB. In spite of the imperfect estimate, the periods of the sinusoidally-vibrating scatterer can still be identified.

5.7.4 MULTI-SCATTERER SIMULATION

Section 5.7.1 refers to a single scatterer which is sinusoidally vibrating. In practice, it is difficult to only have one predominant point scatterer. As an example, the signal coming from the moving chest of a breathing patient may be considered as a combination of different contributions which do not have the same motion amplitude.

Consider one hundred scatterers which are moving sinusoidally in phase, but with different along-LOS range amplitudes. The motion amplitude (R_{pp}) is drawn from a uniform distribution from 0 to 1 cm. Also, the signal amplitude is drawn from an independent uniform random variable from 0 to 1. Fig. 5.21 details the range history extracted from the desired range bin after applying the phase-based method. For comparison purposes, the maximum 1-cm peak-to-peak motion is also indicated.
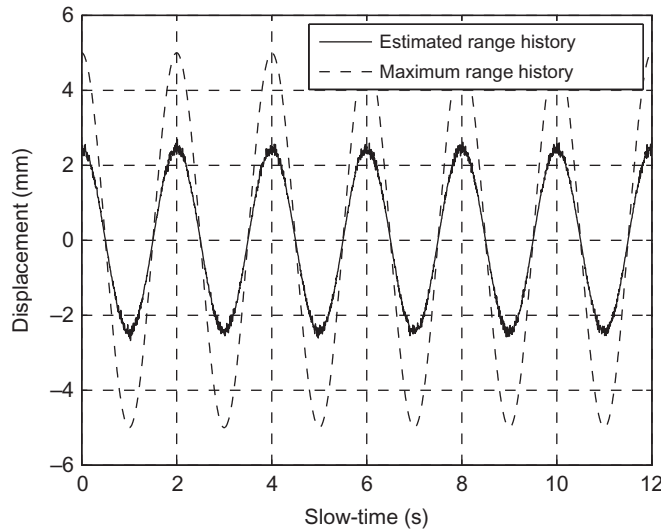

FIGURE 5.21

Range evolutions of multiple in-phase vibrating scatterers. The target-scintillation phenomenon is manifest.

Four important conclusions can be derived from Fig. 5.21. First, the sinusoidal pattern of the motion can be identified, which is encouraging, since the signal is the complex coherent combination of 100 in-phase contributions. Second, the maximum 1-cm peak-to-peak amplitude is not recovered by the algorithm, because many of the scatterers do not fluctuate so much (indeed, the reconstructed amplitude has an approximate value of $R_{pp} = 0.5$ cm). In any case, the desired result is to detect the presence of a motion and hence, the amplitude is unimportant. Third, some negligible noise is observed. Taking into account that the simulated SNR is infinite, the origin of that noise must be found in the aforementioned target-scintillation phenomenon. However, the noise is little, which comes from the fact that the used phase-based method is more robust to this phenomenon than the amplitude-based algorithm, as previously stated in Section 5.3.3. Fourth, the amplitude decrease in Fig. 5.21 corroborates the fact that an energetic stationary clutter scatterer in the same range bin may lead to the impossibility of detecting the wanted motion, as highlighted by Eq. (5.44) and further verified in the next section.

5.7.5 CLUTTER IN THE SAME RANGE BIN

LFMCW radar sensors can easily deal with unwanted targets situated in range bins in which the desired targets are not located. This is why an improvement in the range resolution is normally pursued, so that this range-isolation capability can be further enhanced. Unfortunately, depending on the application, it is sometimes unavoidable to have clutter in the same desired range bin (e.g., if the vital signs of a person are to be monitored, it is almost impossible not to receive echoes from undesired parts, such as head or limbs). If the radar is coherent, the new dimension Doppler can be exploited to devise specific methods which try to mitigate this in-cell unwanted clutter (see Section 5.6).

Consider the scenario shown in Fig. 5.22, which is analogous to the one depicted in Fig. 5.14, with the inclusion of a stationary clutter scatterer at the same distance of the wanted sinusoidally-vibrating target. The radar prototype is assumed to have a center frequency of $f_c = 5.8$ GHz. The transmitted bandwidth is $B = 160$ MHz and the PRF is 500 Hz, whereas the CPI is 12 seconds. The
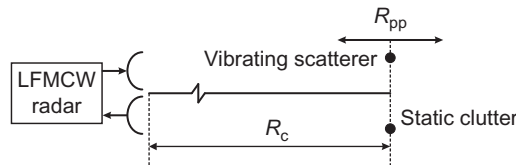

FIGURE 5.22

Simulated scenario for a point-scatterer target sinusoidally vibrating along LOS and a stationary clutter return.

mean range to the targets is $R_c = 5.625$ m, whereas the sinusoidal motion of the desired target is defined through its range amplitude (peak-to-peak $R_{pp} = 50$ cm) and its frequency ($f_t = 0.5$ Hz). The amplitude of the desired target is $K_d = 1$, whereas the amplitude of the clutter scatterer is $K_c = 1.2$.

The slow-time signal for the range bin in which the targets are present can be written as

$$s_b(\tau) = K_d \cdot \exp\left(j\frac{4\pi f_c}{c}\left(R_c + \frac{R_{pp}}{2}\sin(2\pi f_t \tau)\right)\right) + K_c \cdot \exp\left(j\frac{4\pi f_c}{c}R_c\right). \tag{5.47}$$

The second term in Eq. (5.47) is the zero-Doppler clutter component, whereas the first term corresponds to the wanted signal, which has a Doppler frequency, according to Eq. (5.24), given by

$$f_{Dop}(\tau) = -\frac{2\pi f_c f_t R_{pp}}{c}\cos(2\pi f_t \tau). \tag{5.48}$$

For the simulation example in this section, the maximum Doppler frequency can be derived from Eq. (5.48) and turns out to be 30.4 Hz. This value corresponds to the result in Fig. 5.23, which shows the spectrogram for the slow-time signal in the corresponding range bin. The sinusoidal Doppler history associated with the moving target (see Eq. 5.48), together with the zero-Doppler component corresponding to the clutter scatterer, can be seen in Fig. 5.23.

The Fourier transform of the slow-time signal Eq. (5.47) is depicted in magnitude in Fig. 5.24. This figure permits the corroboration of the spectrum distribution shown in Fig. 5.12. It becomes clear that a high-pass filter in the slow-time τ
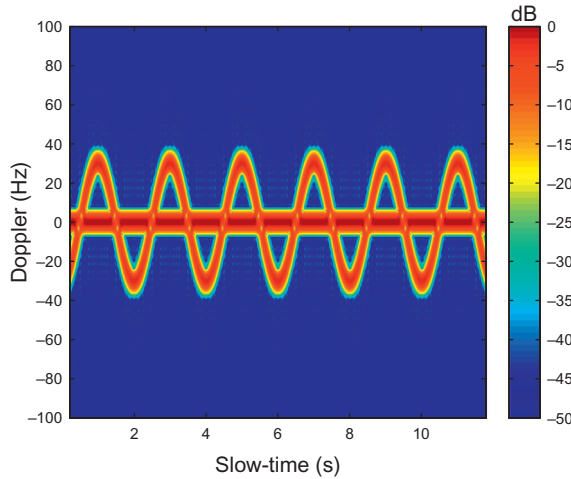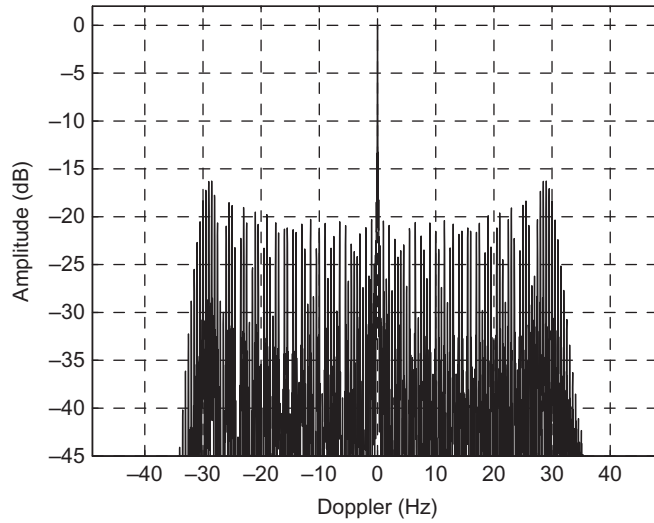

FIGURE 5.23

Spectrogram (Doppler vs slow-time) for a vibrating target and a stationary clutter scatterer.
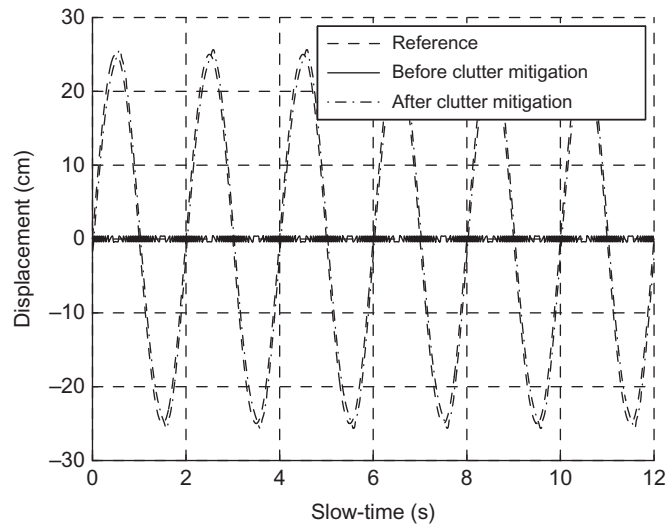
FIGURE 5.24

Doppler spectrum of the simulated slow-time signal for the scenario in Fig. 5.22.

permit the mitigation of the clutter zero-Doppler component at the cost of some distortion added to the desired Doppler spectrum.

The application of the mitigation technique (a fifth-order Chebyshev type-I filter with a 0.5-dB ripple in the passband and a 40-dB attenuation in the 2-Hz-edge-frequency stopband has been employed in this example) permits the recovery of the desired sinusoidal motion of the vibrating scatterer, as shown in Fig. 5.25. Before the mitigation approach of Section 5.6.2, the clutter influence on the desired range history is enormous.

A more compromised simulation considers that the peak-to-peak amplitude is reduced. Assume now that $R_{pp} = 10$ mm. For this situation, the maximum Doppler is only 0.61 Hz, which leads to a desired Doppler spectrum almost identical to DC. Fig. 5.26 shows the range history extracted before and after applying a high-pass filter with cut-off frequency of 0.2 Hz. The ground-truth motion of the wanted target is also shown as a reference. It is true that the sinusoidal pattern is observed before the mitigation technique. However, the Doppler filtering amplifies the displacement amplitude, which may help with the detection of the motion. In any case, due to the added distortion, the amplitude of the estimated range evolution after clutter mitigation does not correspond with the ground-truth 10-mm peak-to-peak amplitude.

As a conclusion, the detection of slow targets when competing with strong stationary clutter is of great difficulty, and any radar in that scenario (e.g., maritime radars trying to detect small and slow boats under heavy clutter) sees its performance degraded.

FIGURE 5.25

Tracked motion pattern for a desired vibrating scatterer before and after applying a clutter-mitigation high-pass filter ($R_{pp} = 50$ cm).
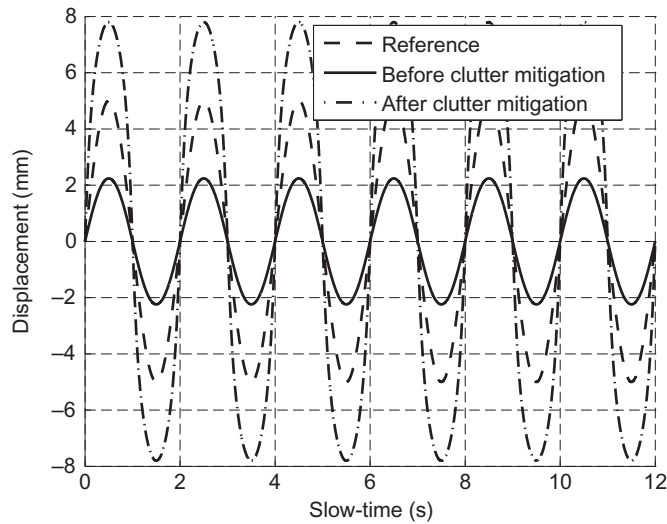
FIGURE 5.26

Tracked motion pattern for a desired vibrating scatterer before and after applying a clutter-mitigation high-pass filter ($R_{pp} = 10$ mm).

5.8 EXPERIMENTAL RESULTS

The suitability of coherent LFMCW radars to short-range human-aware localization applications has also been verified by experimental results. In this section, the radar prototype and some experiments are described to further emphasize the concepts and features around these kinds of systems.

5.8.1 RADAR PROTOTYPE

A block diagram of the developed radar prototype is shown in Fig. 5.27. As can be seen, it uses a deramping-based architecture so that the acquisition block is simple (it works at a reduced sampling frequency of 10 kHz). Some details are given next.

The generation of the ramps is accomplished through the PXIe 5450, which is a baseband vector signal generator able to control the initial phase of each period and to guarantee a high ramp linearity. Its output is upconverted with the PXIe 5611 and PXIe 5652, and is amplified with the PXIe 5691. The final ramp sweeps its frequency from 5.72 to 5.88 GHz, which leads to a transmitted bandwidth of 160 MHz. The waveform period is 2 ms (i.e., a PRF of 500 Hz).

The output of the PXIe 5691 is split through a Wilkinson-type power divider. One output is the signal to be transmitted after a 30-dB gain block, whereas the other one is used as a replica of the transmitted signal in the mixing stage (deramping technique).

In the Rx chain, the signal returned from the targets is amplified. To that purpose, two LNAs and a gain block with a total gain of 47.5 dB are used. The mixer used for the analog deramping is a quadrature mixer, so that the I and Q components of the beat signal are provided at its output. As previously mentioned, the beat signal is acquired with a low-end acquisition block working with a sampling frequency of 10 kHz. The samples of the beat signal are stored for further off-line processing.

The architecture uses a two-antenna scheme, which consists of two 2×2 planar patch arrays, so that the isolation between them can be small. The inclusion of two delay lines permits keeping the desired beat frequency far from the low-frequency baseband spectrum, which is usually contaminated with strong flicker noise. The extra delay added by the lines can be easily compensated for through calibration.

Finally, the coherence of the radar is guaranteed by sharing a common clock between the generation and acquisition blocks, as expounded in Section 5.3.2. Two photographs of the prototype are provided in Fig. 5.28, with the interconnection details in Fig. 5.28(B).

Fig. 5.29 schematically depicts the experimental setups made with the radar prototype, which are respectively associated with the next sections.
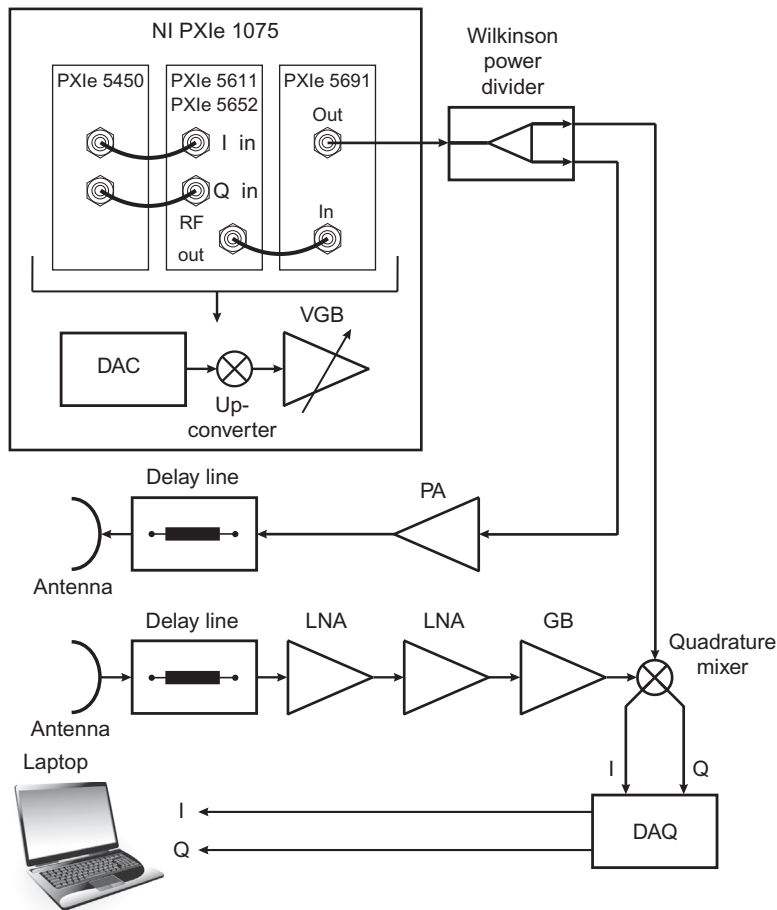
FIGURE 5.27

Block diagram for the coherent C-band LFMCW radar prototype (power amplifier: PA; low-noise amplifier: LNA; digital-to-analog converter: DAC; data acquisition: DAQ; gain block: GB; variable gain block: VGB).

5.8.2 ABSOLUTE RANGE MEASURES OF METAL PLATES

In this experiment, a metal plate on a small cart is perpendicularly located at different ranges from the radar (see Fig. 5.29(A)). The range position of the plate is estimated through the amplitude-based method, which obtains the position of the corresponding peak observed in the frequency domain of the beat signal. The calibration distance was set at 4.5 ft (137.16 cm). Fig. 5.30 shows the spectrum of the beat signal when the metal plate was situated at 4.5 ft and at 8.5 ft. In addition to the echo associated with the desired target, some peaks corresponding to clutter
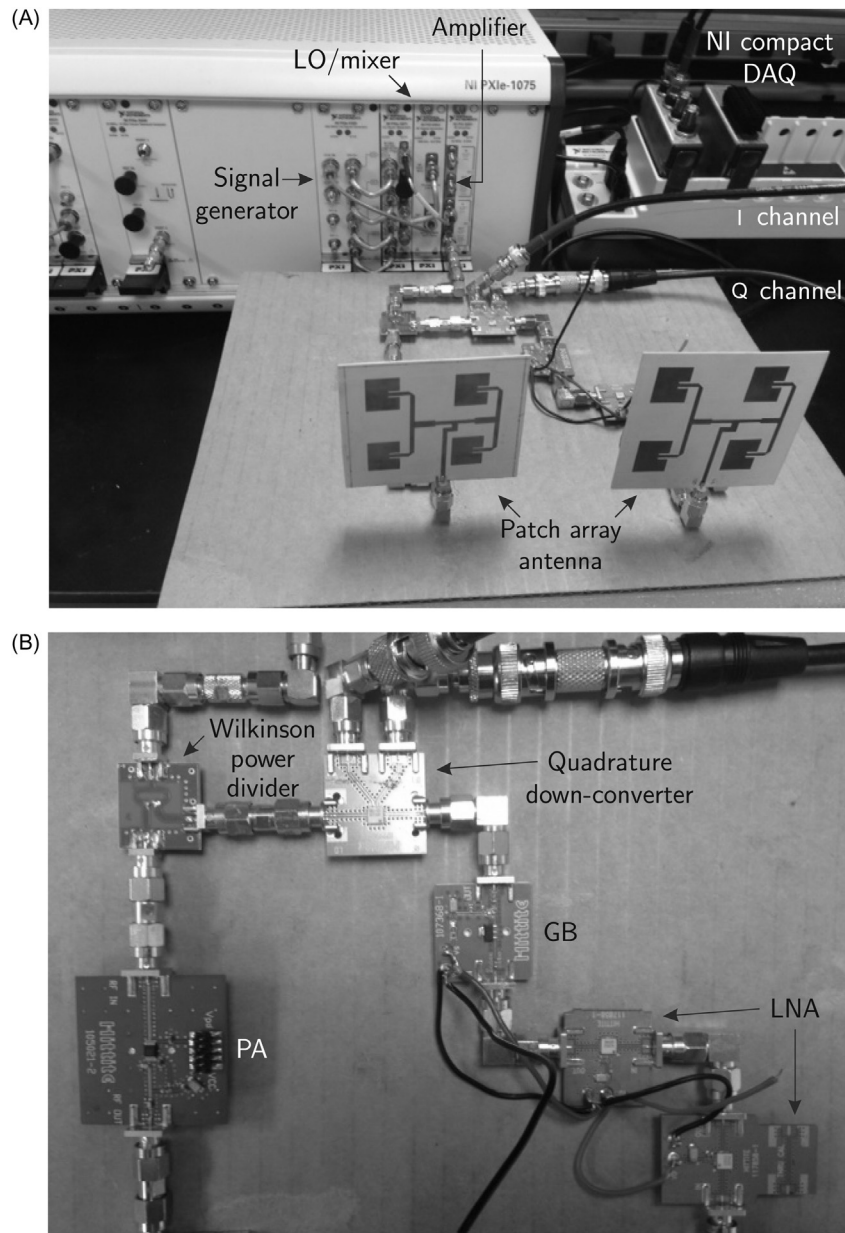
FIGURE 5.28

Photograph of the coherent C-band LFMCW radar prototype (power amplifier: PA; low-noise amplifier: LNA; digital-to-analog converter: DAC; data acquisition: DAQ; gain block: GB; local oscillator: LO). (A) Overall view. (B) RF detail.
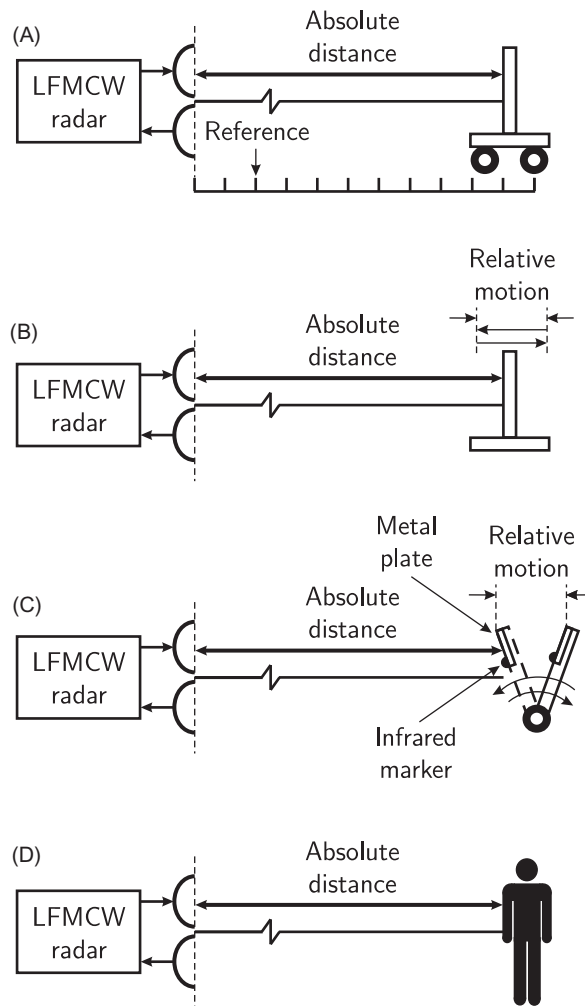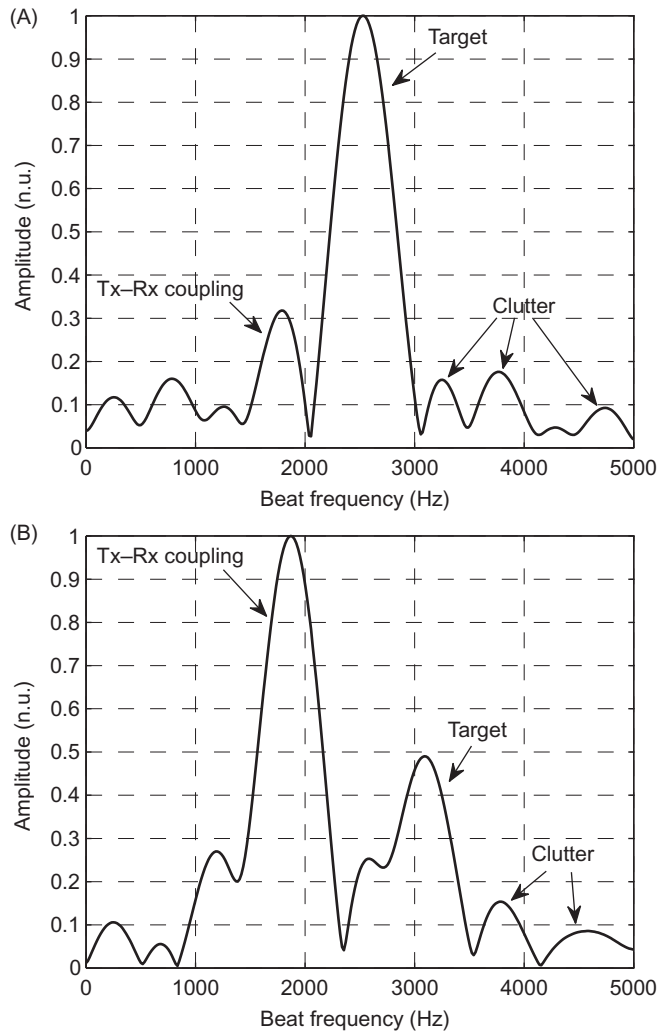
FIGURE 5.29

Schematic representations of the experimental setups. (A) Absolute ranging of a metal plate. (B) Tracking of the range history of a sinusoidally-vibrating metal plate. (C) Tracking of the range history of a phantom-borne metal plate with stop periods. (D) Monitoring of vital signs.

are observed. The Tx–Rx coupling requires special mention, since it means a powerful return, which may be even greater than that associated with the metal plate (especially when the target is far from the radar, and thus the wanted received power is lower). This powerful Tx–Rx coupling means large sidelobes, which may mask desired weak targets, and calls for a redesign of the antennas so that the Tx–Rx isolation may be improved.

FIGURE 5.30

Beat-signal spectrum magnitude for a metal plate situated at the calibration distance of 4.5 ft (A), and at a range of 8.5 ft (B).

Table 5.2 details the absolute range measures of the metal plate at different locations. As seen, a systematic error is observed for every position, which limits the accuracy of the system. Related with the discussions in Section 5.5.3, the origin of this biasing may be found in the high interference of the Tx−Rx coupling, or in the fact that a metal plate is a good scatterer, but cannot be considered a point scatterer.

Table 5.2 Experimental Absolute Range Measurements and Associated
Errors [25]

Reference Distance (ft/cm)	Beat Frequency (Hz)	Measured Distance (ft/cm)	Associated Error (ft/cm)
3.0/91.44	2305.8	3.11/94.79	+0.11/ + 3.35
3.5/106.68	2401.1	3.69/112.47	+0.19/ + 5.79
4.0/121.92	2456.1	4.03/122.83	+0.03/ + 0.91
4.5/137.16	2531.3	4.50/137.16	0.00/0.00
5.0/152.40	2606.5	4.96/151.18	−0.04/ − 1.22
5.5/167.64	2656.6	5.27/160.63	−0.23/ − 7.01
6.0/182.88	2731.8	5.73/174.65	−0.27/ − 8.23
6.5/198.12	2807.0	6.19/188.67	−0.31/ − 9.45
7.0/213.36	2882.2	6.66/203.00	−0.44/ − 13.41
7.5/228.60	2957.6	7.12/217.02	−0.43/ − 13.11
8.0/243.84	3022.4	7.52/229.21	−0.48/ − 14.63
8.5/259.08	3105.3	8.03/244.75	−0.47/ − 14.32
9.0/274.32	3222.2	8.75/266.70	−0.25/ − 7.62
9.5/289.56	3272.0	9.16/279.20	−0.34/ − 10.36
10.0/304.80	3339.1	9.57/291.69	−0.43/ − 13.11
10.5/320.40	3406.0	10.08/307.24	−0.42/ − 12.80
11.0/335.28	3523.0	10.60/323.09	−0.40/ − 12.19
11.5/350.52	3606.0	11.11/338.63	−0.39/ − 11.89
12.0/365.76	3673.0	11.62/354.18	−0.38/ − 11.58

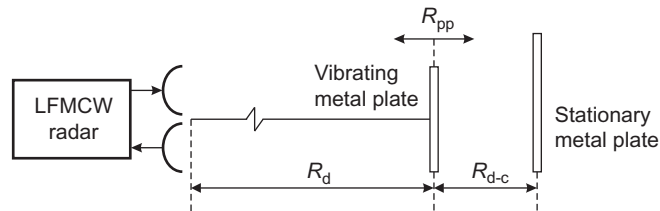### 5.8.3 RANGE TRACKING OF A VIBRATING METAL PLATE

The metal plate is now situated in an actuator which generates a sinusoidal
motion with a peak-to-peak amplitude of 1.5 cm and a period of 4.762 seconds
(see Fig. 5.29(B)). After applying the phase-based method in Section 5.4.3 to
track the motion of the metal plate, the results are depicted in Fig. 5.31. As can
be checked, the tracking accuracy is less than 1 mm, although it must again be
emphasized than the metal plate is not a point scatterer and the real actuator does
not have an infinite precision.

Fig. 5.32 shows the same scenario of Fig. 5.29(B), with the inclusion of a sta-
tionary metal plate which emulates strong clutter returns at the same range bin.
Referring to the nomenclature in Fig. 5.32, the mean range to the desired target is
$R_d = 2$ m. Now, the actuator generates a sinusoidal motion with a peak-to-peak
amplitude $R_{pp} = 2$ cm and a period of 3 seconds. The range separation between
the vibrating metal plate and the stationary one is $R_{d-c} = 20$ cm.

The tracked motion of the vibrating metal plate before and after applying a
high-pass filter with a cut-off frequency of 0.2 Hz is shown in Fig. 5.33. For this
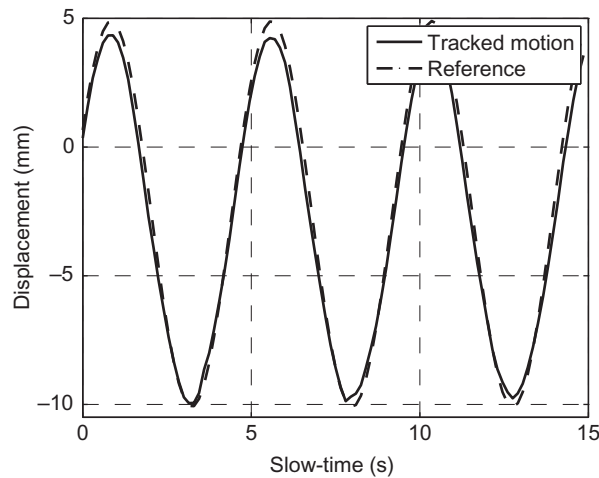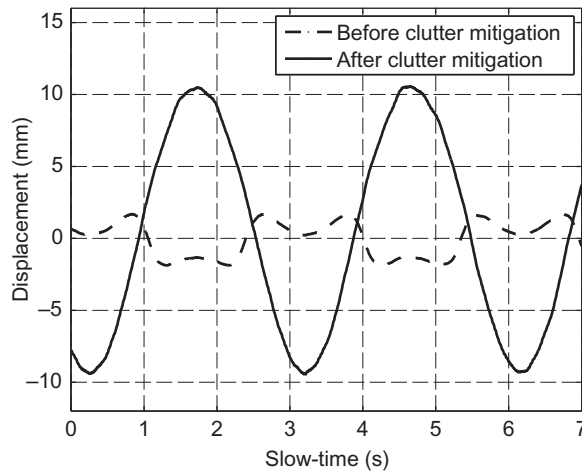
FIGURE 5.31

Experimental range evolution extracted for an along-LOS sinusoidally-vibrating metal plate.
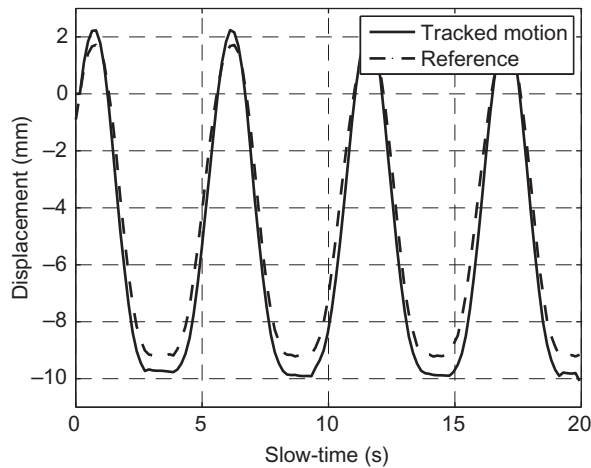

FIGURE 5.32

Experimental scenario for a sinusoidally-vibrating metal plate and a clutter-assumed stationary metal plate.

particular example, the clutter-mitigation technique is effective and enables a correct tracking of the desired motion.

As mentioned, Doppler radars usually require complex architectures to follow DC components of the desired signal. These DC components are present in practical signals, such as vital signs. The proposed coherent LFMCW architecture is simple and also permits the maintaining of the DC structure of the wanted signal. To experimentally verify this feature, the metal plate was mounted on a professional phantom which mimics the chest movement (see Fig. 5.29(C)). Fig. 5.34 shows the detected motion pattern of the metal plate. As seen, the motion is tracked even during the stop periods of the phantom motion. Fig. 5.34 also shows a reference motion based on an infrared marker. A fair agreement between both motions is observed.
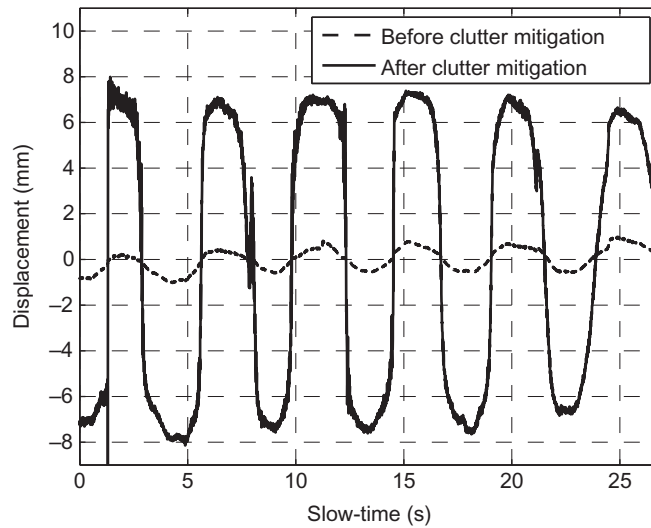
FIGURE 5.33

Range evolution extracted for an along-LOS sinusoidally-vibrating metal plate before and after applying the clutter-mitigation high-pass filtering.
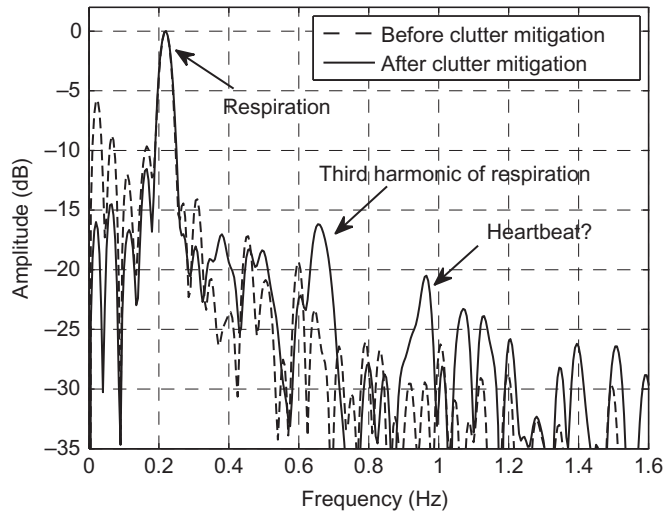

FIGURE 5.34

Tracked motion and infrared-based reference for a phantom-borne metal plate.

5.8.4 MONITORING OF VITAL SIGNS

The coherent short-range LFMCW radar prototype was also used to illuminate a breathing subject (see Fig. 5.29(D)). The patient was sitting in front of the radar and was normally breathing.

FIGURE 5.35

Range tracking of vital signs before and after applying the clutter-mitigation approach.

FIGURE 5.36

Fourier transform of the range histories corresponding to the experimental vital sign monitoring scenario before and after clutter-mitigation high-pass filtering.

Fig. 5.35 shows the tracked signal before and after applying a high-pass filter with a cut-off frequency of 0.1 Hz. Note that the vital sign is extremely slow. Indeed, by supposing an approximate breathing period of 4.5 seconds and a peak-to-peak amplitude of the respiration signal of 15 mm, the maximum Doppler frequency is only 0.4 Hz. Additionally, the vital sign is weak, when compared with the echoes coming from the metal plates. This makes the tracking of vital signs extremely challenging.

As shown in Fig. 5.35, the mitigation technique permits the enhancement of the amplitude of the vital sign. After applying a Fourier transform to that signal, the frequency components of the vital sign can be distinguished (see Fig. 5.36). The results in Fig. 5.36 indicate that the Doppler high-pass filtering is effective in cleaning the spectrum, and thus even the heartbeat signal appears to be detectable.

5.9 FURTHER WORK

Coherent LFMCW radar systems are interesting devices for short-range human-aware localization applications. From our point of view, moving to high-frequency devices (e.g., millimeter-wave radars) is the next step. Reasons are indicated in the following:

- A higher absolute bandwidth can be transmitted. This means that a higher range resolution can be achieved, and thus better range-isolation capabilities can be accomplished.
- A higher range precision for the phase-based method can be obtained, according to Eq. (5.33). A look should be taken at the phase-unwrapping process, which may be more complex.
- The antennas can have a greater directivity. This leads to a better Tx−Rx isolation and to a better concentration of the radiation on the desired target (thus diminishing the clutter contributions).
- The Doppler frequencies would be increased. This means that the under-study slow signals would be filtered more easily in the Doppler domain.

ACKNOWLEDGMENTS

REFERENCES

[1] Charvat GL, Williams J, Zeng S, Nickalaou J. Small and short-range radar systems. Taylor & Francis; 2014.

[2] Muñoz-Ferreras JM, Pérez-Martínez F, Calvo-Gallego J, Asensio-López A, Dorta-Naranjo BP, Blanco-del-Campo A. Traffic surveillance system based on a high resolution radar. IEEE Trans Geosci Remote Sens 2008;46(6):1624−33.

[3] Ayhan S, Scherr S, Pahl P, Kayser T, Pauli M, Zwick T. High-accuracy range detection radar sensor for hydraulic cylinders. IEEE Sens J 2014;14(3):734−46.

[4] Armbrecht G, Zietz C, Denicke E, Rolfes I. Antenna impact on the gauging accuracy of industrial radar level measurements. IEEE Trans Microw Theory Techn 2011;59 (10):2554−62.

[5] Felguera-Martín D, González-Partida JT, Almorox-González P, Burgos-García M. Vehicular traffic surveillance and road lane detection using radar interferometry. IEEE Trans Veh Technol 2012;61(3):959−70.

[6] Raj RG, Chen VC, Lipps R. Analysis of radar human gait signatures. IET Signal Processing. 2010;4(3):234−44.

[7] Wang FK, Horng TS, Peng KC, Jau JK, Li JY, Chen CC. Detection of concealed individuals based on their vital signs by using a see-through-wall imaging system with a self-injection-locked radar. IEEE Trans Microw Theory Techn 2013;61 (1):696−704.

[8] Nanzer JA, Anderson MG, Josser TM, Li K, Olinger GA, Buhl DP, et al. Detection of moving intruders from a moving platform using a Ka-band continuous-wave Doppler radar. In: Proceedings IEEE Antennas Propagation Society International Symposium, Charleston, SC, USA, June 2009, pp. 1−4.

[9] Mercuri M, Schreurs D, Leroux P. SFCW microwave radar for in-door fall detection. In: Proceedings of IEEE Topical Conference Biomedical Wireless Technologies, Networks, Sensing Systems, Santa Clara, CA, USA, January 2012, pp. 53−56.

[10] Amin MG, Ahmad F. Change detection analysis of humans moving behind walls. IEEE Trans Aerosp Electron Syst 2013;49(3):1410−25.

[11] Li C, Lubecke VM, Boric-Lubecke O, Lin J. A review on recent advances in Doppler radar sensors for noncontact healthcare monitoring. IEEE Trans Microw Theory Techn 2013;61(5):2046−60.

[12] Schleicher B, Nasr I, Trasser A, Schumacher H. IR-UWB radar demonstrator for ultra-fine movement detection and vital-sign monitoring. IEEE Trans Microw Theory Techn 2013;61(5):2076−85.

[13] Hafner N, Mostafanezhad I, Lubecke VM, Boric-Lubecke O, Host-Madsen A. Noncontact cardiopulmonary sensing with a baby monitor. In: Proceedings of 29th Annual International Conference IEEE Engineering in Medicine and Biology Society, Lyon, France, August 2007, pp. 2300−2.

[14] Gu C, Li R, Zhang H, Fung AYC, Torres C, Jiang SB, et al. Accurate respiration measurement using DC-coupled continuous-wave radar sensor for motion-adaptive cancer radiotherapy. IEEE Trans Biomed Eng 2012;59(11):3117−23.

[15] Li C, Lin J, Xiao Y. Robust overnight monitoring of human vital signs by a noncontact respiration and heartbeat detector. In: Proceedings of 28th Annual International Conference IEEE Engineering in Medicine and Biology Society, New York, NY, USA, August 2006, pp. 2235−8.

[16] Morinaga M, Nagasaku T, Shinoda H, Kondoh H. 24-GHz intruder detection radar with beam-switched area coverage. In: Proceedings of IEEE MTT-S International Microwave Symposium, Honolulu, HI, USA, June 2007, pp. 389−92.

[17] Li C, Gu C, Li R, Jiang SB. Radar motion sensing for accurate tumor tracking in radiation therapy. In: Proceedings of IEEE 12th Annual Wireless Microwave Technology Conference, 2011, pp. 1−6.

[18] Wang J, Wang X, Zhu Z, Huangfu J, Li C, Ran L. 1-D microwave imaging of human cardiac motion: an AB-initio investigation. IEEE Trans Microw Theory Techn 2013;61(5):2101−7.

[19] Zito D, Pepe D, Mincica M, Zito F, Tognetti A, Lanata A, et al. SoC CMOS UWB pulse radar sensor for contactless respiratory rate monitoring. IEEE Trans Biomed Circuits Syst 2011;5(6):503−10.

[20] Gezici S. Theoretical limits for estimation of periodic movements in pulse-based UWB systems. IEEE J Sel Top Signal Process 2007;1(3):405−17.

[21] Bernardi P, Cicchetti R, Pisa S, Pittella E, Piuzzi E, Testa O. Design, realization, and test of a UWB radar sensor for breath activity monitoring. IEEE Sens J 2014;14(2):584−96.

[22] Zhang C, Kuhn MJ, Merkl BC, Fathy AE, Mahfouz MR. Real-time noncoherent UWB positioning radar with millimeter range accuracy: theory and experiment. IEEE Trans Microw Theory Techn 2010;58(1):9−20.

[23] Wang G, Gu C, Inoue T, Li C, Hybrid FMCW-interferometry radar system in the 5.8 GHz ISM band for indoor precise position and motion detection. In: Proceedings of IEEE MTT-S International Microwave Symposium, Seattle, WA, USA, June 2013, pp. 1−3.

[24] Wang G, Muñoz-Ferreras JM, Gu C, Li C, Gómez-García R. Linear-frequency-modulated continuous-wave radar for vital-sign monitoring. In: Proceedings of IEEE Topical Conference Biomedical Wireless Technologies, Networks, Sensing Systems, Newport Beach, CA, USA, January 2014, pp. 1−3.

[25] Wang G, Muñoz-Ferreras JM, Gu C, Li C, Gómez-García R. Application of linear-frequency-modulated continuous-wave (LFMCW) radars for tracking of vital signs. IEEE Trans Microw Theory Techn 2014;62(6):1387−99.

[26] Wang G, Gu C, Inoue T, Li C. A hybrid FMCW-interferometry radar for indoor precise positioning and versatile life activity monitoring. IEEE Trans Microw Theory Techn 2014;62(11):2812−22.

[27] Belyaev E, Molchanov P, Vinel A, Koucheryavy Y. The use of automotive radars in video-based overtaking assistance applications. IEEE Trans Intell Transp Syst 2013;14(6):1035−42.

[28] Feger R, Pfeffer C, Scheiblhofer W, Schmid CM, Lang MJ, Stelzer A. A 77-GHz cooperative radar system based on multi-channel FMCW stations for local positioning applications. IEEE Trans Microw Theory Techn 2013;61(1):676−84.

[29] Luo T-N, Wu C-HE, Chen Y-JE. A 77-GHz CMOS FMCW frequency synthesizer with reconfigurable chirps. IEEE Trans Microw Theory Techn 2013;61(7):2641−7.

[30] Richards MA, Scheer JA, Holm WA. Principles of modern radar: basic principles. 2nd ed. Edison, NJ: SciTech Publishing; 2010.

[31] Skolnik MI. Introduction to radar systems. 3rd ed. New York, NY: McGraw-Hill; 2002.

[32] Carrara WG, Goodman RS, Majewski RM. Spotlight synthetic aperture radar: signal processing algorithms. Boston, MA: Artech House; 1995.

[33] Wehner DR. High-resolution radar. 2nd ed. Boston, MA: Artech House; 1995.

[34] Edrich M. Design overview and flight test results of the miniaturised SAR sensor MISAR. Proceedings of 1st European Radar Conference. Amsterdam, The Netherlands; 2004. p. 205−8.

[35] Almorox-Gonzalez P, González-Partida JT, Burgos-García M, de la Morena-Álvarez-Palencia C, Arche-Andradas L, Dorta-Naranjo BP. Portable high resolution LFM-CW radar sensor in millimeter-wave band. In: Proceedings of International Conference Sensor Technologies and Applications, Valencia, Spain, October 2007, pp. 5−9.

[36] Zaugg EC, Long DG. Theory and application of motion compensation for LFM-CW SAR. IEEE Trans Geosci Remote Sens 2008;46(10):2990−8.

[37] Zaugg EC, Hudson DL, Long DG. The BYU μSAR: a small, student-built SAR for UAV operation. In: Proceedings of IEEE International Geoscience Remote Sensing Symposium, Denver, CO, USA, August 2006, pp. 411−14.

[38] Meta A, de Wit JJM, Hoogeboom P. Development of a high resolution airborne millimeter wave FM-CW SAR. In: Proceedings of 1st European Radar Conference, Amsterdam, The Netherlands, October 2004, pp. 209−12.

[39] Muñoz-Ferreras JM, Pérez-Martínez F, Burgos-García M. Helicopter classification with a high resolution LFMCW radar. IEEE Trans Aerosp Electron Syst 2009;45(4):1373−84.

[40] Wang J, Kasilingam D. Global range alignment for ISAR. IEEE Trans Aerosp Electron Syst 2003;39(1):351−7.

[41] Muñoz-Ferreras JM, Pérez-Martínez F. Subinteger range-bin alignment method for ISAR imaging of noncooperative targets. EURASIP J Adv Signal Processing 2010;2010(1):1−16.

[42] Chen VC. The micro-doppler effect in radar. Norwood, MA: Artech House; 2011.

[43] Muñoz-Ferreras JM, Pérez-Martínez F. Superresolution versus motion compensation-based techniques for radar imaging defense applications. EURASIP J Adv Signal Processing 2010;2010(1):1−9.

[44] Brennan PV, Lok LB, Nicholls K, Corr H. Phase-sensitive FMCW radar system for high-precision Antarctic ice shelf profile monitoring. IET Radar Sonar Navig. 2014;8(7):776−86.

[45] Wang G, Muñoz-Ferreras JM, Gómez-García R, Li C. Clutter interference reduction in coherent FMCW radar for weak physiological signal detection. In: Proceedings of IEEE MTT-S International Microwave Symposium, Tampa Bay, FL, USA, 2014, pp. 1−3.

[46] Muñoz-Ferreras JM, Wang G, Li C, Gómez-García R. Mitigation of stationary clutter in vital-sign-monitoring linear-frequency-modulated continuous-wave radars. IET Radar Sonar Navig 2015;9(2):138−44.

[47] Muñoz-Ferreras JM, Peng Z, Gómez-García R, Wang G, Gu C, Li C. Isolate the clutter: pure and hybrid linear-frequency-modulated continuous-wave (LFMCW) radars for indoor applications. IEEE Microw Mag 2015;16(4):40−54.